Mineralium Deposita (2018) 53:1039–1060
https://doi.org/10.1007/s00126-018-0794-4

ARTICLE

Origin of the volcanic-hosted Yamansu Fe deposit, Eastern Tianshan, NW China: constraints from pyrite Re-Os isotopes, stable isotopes, and in situ magnetite trace elements

Xiao-Wen Huang[1,2] · Mei-Fu Zhou[3] · Georges Beaudoin[2] · Jian-Feng Gao[1] · Liang Qi[1] · Chuan Lyu[1,4]

Received: 14 June 2017 / Accepted: 15 January 2018 / Published online: 31 January 2018

Abstract

The Yamansu Fe deposit (32 Mt at 51% Fe) in the Eastern Tianshan Orogenic Belt of NW China is hosted in early Carboniferous volcano-sedimentary rocks and spatially associated with skarn. The paragenetic sequence includes garnet-diopside (I), magnetite (II), hydrous silicate-sulfide (III), and calcite-quartz (IV) stages. Pyrite associated with magnetite has a Re-Os isochron age of 322 ± 7 Ma, which represents the timing of pyrite and, by inference, magnetite mineralization. Pyrite has $\delta^{34}S_{VCDT}$ values of − 2.2 to + 2.9‰, yielding $\delta^{34}S_{H2S}$ values of − 3.1 to 2‰, indicating the derivation of sulfur from a magmatic source. Calcite from stages II and IV has $\delta^{13}C_{VPDB}$ values from − 2.5 to − 1.2‰, and − 1.1 to 1.1‰, and $\delta^{18}O_{VSMOW}$ values from 11.8 to 12.0‰ and − 7.7 to − 5.2‰, respectively. Calculated $\delta^{13}C$ values of fluid CO_2 and water $\delta^{18}O$ values indicate that stage II hydrothermal fluids were derived from magmatic rocks and that meteoric water mixed with the hydrothermal fluids in stage IV. Some ores contain magnetite with obvious chemical zoning composed of dark and light domains in BSE images. Dark domains have higher Mg, Al, Ca, Mn, and Ti but lower Fe and Cr contents than light domains. The chemical zoning resulted from a fluctuating fluid composition and/or physicochemical conditions (oscillatory zoning), or dissolution-precipitation (irregular zoning) via infiltration of magmatic-hydrothermal fluids diluted by late meteoric water. Iron was mainly derived from fluids similar to that in skarn deposits.

Keywords Re-Os geochronology · Trace elements · Magnetite · Dissolution-reprecipitation · Yamansu Fe deposit

Introduction

The Paleozoic Tianshan Orogenic Belt (TOB), NW China, has been a focus of mineral exploration in China (Wang et al. 2006a). Particularly, the Chagangnuoer, Beizhan, Dunde, and Zhibo Fe deposits are well known in the western part of the TOB (Hou et al. 2014a; Zhang et al. 2014) and the Yamansu, Heifengshan, Shuangfengshan, and Shaquanzi Fe deposits in its eastern part (Gao et al. 1993; Che et al. 1994; Qin et al. 2002; Wang et al. 2006a; Huang et al. 2013a, 2014a, b). These deposits were thought to be submarine volcanogenic in origin because they are hosted in volcanic rocks (Jiang 1983; Jiang and Wang 2005). They are also considered to be related to skarnization because of extensive skarn alteration and associated with concealed intrusions (Mao et al. 2005; Pirajno 2010), although they are different from typical skarn deposits in that they are not directly in contact with intrusions (Einaudi et al. 1981). The Yamansu deposit contains 32 Mt at

Editorial handling: R. Hu

Electronic supplementary material The online version of this article (https://doi.org/10.1007/s00126-018-0794-4) contains supplementary material, which is available to authorized users.

✉ Mei-Fu Zhou
mfzhou@hku.hk

[1] State Key Laboratory of Ore Deposit Geochemistry, Institute of Geochemistry, Chinese Academy of Sciences, Guiyang 550081, China

[2] Département de géologie et de génie géologique, Université Laval, Quebec City, QC G1V0A6, Canada

[3] Department of Earth Sciences, The University of Hong Kong, Hong Kong, SAR, China

[4] University of Chinese Academy of Sciences, Beijing 100049, China

51% Fe (Mao et al. 2005) and is one of the largest Fe deposits in the eastern TOB. This deposit has many geological, mineralogical, and geochemical features similar to other alkali-calcic, hydrothermally altered volcanic rock-hosted Fe deposits, which are the subject of a long-standing debate concerning a possible magmatic or hydrothermal origin, or a combination of both (Henriquez and Martin 1978; Nyström and Henríquez 1994; Rhodes et al. 1999; Sillitoe and Burrows 2002; Nyström et al. 2008; Dare et al. 2015; Zhang et al. 2015; Tornos et al. 2016; Günther et al. 2017; Tang et al. 2017; Zheng et al. 2017). For example, recent studies of in situ trace elements and iron isotopes of magnetite from the Zhibo and Chagangnuoer Fe deposits demonstrated a combined orthomagmatic and skarn process for the formation of these deposits (Günther et al. 2017). However, the timing of mineralization, origin and evolution of hydrothermal fluids, and iron enrichment mechanism of the Yamansu deposit are still lacking. Therefore, detailed studies of the Yamansu deposit will provide important constraints on the origin of volcanic rock-hosted Fe deposits in the TOB.

In this study, we describe the field relationships, paragenetic sequence, and mineralization styles of the Yamansu deposit. Pyrite Re-Os geochronology is used to date pyrite that is associated with magnetite. Carbon and oxygen isotope compositions of calcite and sulfur isotope composition of pyrite, together with in situ trace element composition of magnetite, are used to constrain the origin and evolution of the hydrothermal fluids and the mechanism of iron enrichment in the Yamansu deposit. The implications for the regional Fe(-Cu) metallogeny in the ETOB are also discussed.

Regional geology

The Central Asian Orogenic Belt (CAOB) is the largest Phanerozoic orogen in the world, extending ~ 7000 km from west to east, and is a complex collage of continental fragments, island arc assemblages, remnants of oceanic crust, and continental margins between the Siberian Craton to the north and the Tarim-North China Craton to the south (Fig. 1a). It was formed by multiple subduction-accretion and collision processes from the Neoproterozoic to the Late Paleozoic (Sengör and Burtman 1993; Jahn et al. 2000; Windley et al. 2007; Xiao et al. 2008). The TOB in the southern CAOB extends from northern Xinjiang to Gansu for more than 3000 km (Fig. 1b). The eastern part of the TOB (ETOB) comprises four main tectonic units from north to south, the Dananhu-Tousuquan, Kanggurtag, Aqishan-Yamansu, and Central Tianshan belts (Fig. 1c) (He et al. 1994; Gao et al. 1998; Qin et al. 2002; Xiao et al. 2004; Wang et al. 2006b).

The Dananhu-Tousuquan belt is composed of Devonian to Carboniferous island arc volcanic rocks. Devonian rocks, basaltic to andesitic volcanic rocks, are locally associated with carbonate and calcareous mudstone. Overlying these rocks is the late Carboniferous Tuwu Formation, composed of greywacke and tuff intercalated with carbonates. The Tuwu Formation is overlain by Permian basalt, tuff and volcanic breccia, and Jurassic terrestrial clastic rocks (Mao et al. 2005).

In the Kanggurtag belt, there are mylonite, tectonic lenses, and breccias formed along early compressional faults (Qin et al. 2002; Xu et al. 2003). The Carboniferous strata consist of fine-grained sandstone and carbonaceous argillite. The Kanggurtag belt contains ophiolitic fragments and was thought to mark a suture zone separating the Siberia craton to the north from the Tarim block to the south (Ji et al. 1994; Yang et al. 1996; Ma et al. 1997; Zhou et al. 2001). The Kanggurtag belt was also thought to be an inter-arc basin between the Dananhu-Tousuquan and Yamansu arcs (Ma et al. 1997; Shu et al. 2002).

The Aqishan-Yamansu belt is separated by the Kushui fault from the Kanggurtag belt to the north and by the Shaquanzi fault from Central Tianshan belt to the south. In the Aqishan-Yamansu belt, the lower Carboniferous Yamansu Formation is composed of a 5-km-thick succession of bimodal volcanic rocks, the middle Carboniferous Shaquanzi Formation of the clastic rocks and andesitic tuff, and the upper Carboniferous Tugutublak Formation of intercalated carbonate and volcanic rocks. There are also Permian marine and terrestrial clastic rocks intercalated with bimodal volcanic rocks and carbonates (Mao et al. 2005). Dacite and rhyolite of the Yamansu Formation in the east, middle, and western parts of ETOB have zircon U-Pb ages of 348.0 ± 1.7, 335.9 ± 2.4, and 334.0 ± 2.5 Ma, respectively (Luo et al. 2012). Rhyolite of the Shaquanzi Formation has a zircon U-Pb age of 320 ± 1.2 Ma (Li et al. 2011). This belt was thought to be an island arc belt (Yan 1985; Ma et al. 1997; Yang et al. 1999). However, it has also been interpreted to be an early Carboniferous rift zone because of widespread intraplate rift-related volcanic rocks (Xiao et al. 1992; Qin et al. 2002; Xia et al. 2003). Iron deposits in this belt include the larger Yamansu deposit, the smaller Heifengshan, Shuangfengshan, Shaquanzi, Bailingshan, and Hongyuntan deposits (Fig. 1c).

The Central Tianshan belt in the ETOB has been regarded as a composite volcanic arc, composed of Precambrian basement rocks of amphibolite facies, overlain by calc-alkaline basaltic andesite, volcanoclastic rocks, intruded by minor I-type granite and granodiorite (Xiao et al. 2004). The Precambrian basement consists of gneiss, quartz schist, migmatite, and marble. Iron deposits in this belt are represented by the Precambrian metamorphic rocks hosted Tianhu deposit (Huang et al. 2015; Wu et al. 2016) and Permian alkaline gabbro complex hosted Weiya magmatic Fe-Ti-V deposit (Wang et al. 2005; Zhang et al. 2005).

Large volumes of Carboniferous to Permian granitic rocks in the ETOB include quartz diorite, granodiorite, monzonite, biotite granite, and K-feldspar granite (Tong et al. 2010; Zhou

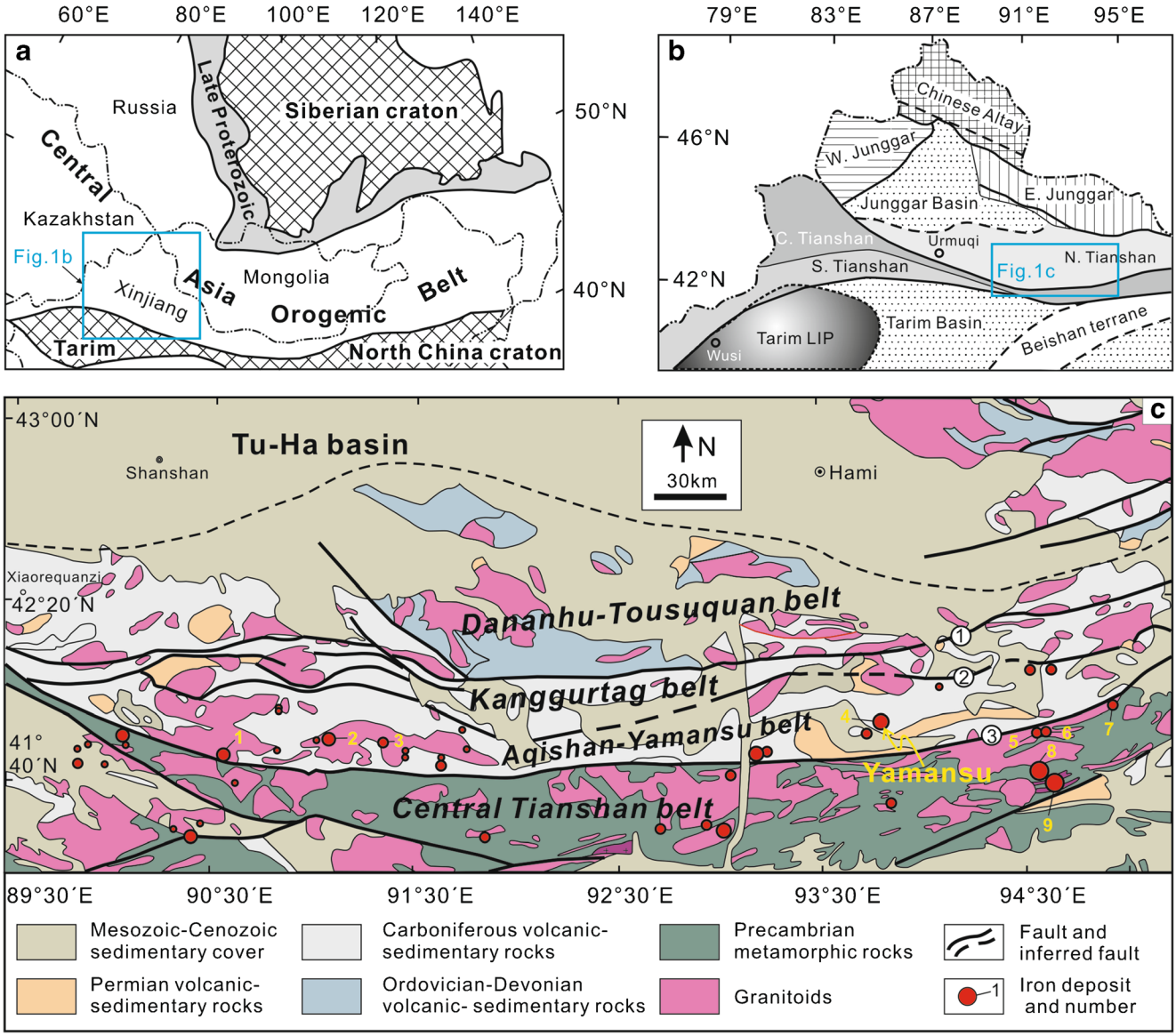

Fig. 1 **a** Location of the study area in the Central Asia Orogenic Belt (modified from Zhang et al. 2009). **b** Sketch map showing geologic units of northern Xinjiang, NW China (modified from Xie et al. 2012). **c** Regional geological map of the Eastern Tianshan Orogenic Belt (modified from Wang et al. 2006b). Faults: ①—Kanggurtag-Huangshan fault, ②—Kushui fault, ③—Shaquanzi fault. Iron deposits: 1—Hongyuntan, 2—Tieling, 3—Bailingshan, 4—Yamansu, 5—Heifengshan, 6—Shuangfengshan, 7—Shaquanzi, 8—Weiya, 9—Tianhu

et al. 2010). There are numerous Permian mafic and ultramafic intrusions in the Kanggurtag belt, including the Huangshan, Xiangshan, and Hulu intrusions (Qin et al. 2003; Han et al. 2004; Zhou et al. 2004).

Geology of the Yamansu deposit

In the Yamansu ore district, the host rocks include the lower Carboniferous Yamansu Formation and the upper Carboniferous Shaquanzi Formation (Fig. 2). The Yamansu Formation comprises andesitic tuff and andesitic volcanic breccia intercalated with limestone in the upper unit and volcanic and volcanic-clastic rocks in the lower unit. The upper unit hosts iron mineralization (Fig. 2). Hou et al. (2014b) obtained a zircon age of 324.4 ± 0.94 Ma for basalt of the Yamansu Formation in the Yamansu deposit. The Shaquanzi Formation comprises flysch intercalated with bimodal volcanic and carbonate rocks and is overlain by Lower Permian marine and terrestrial clastic rocks (Mao et al. 2005). Four major NNE- to NEE-trending faults have been recognized in the ore district (Fig. 3a). Among them, post-ore faults, F_2 and F_8, crosscut and displaced the orebodies (Fig. 3).

The Yamansu deposit is intruded by some subvolcanic pyroxene-diorite porphyries, cropping out about 500 m southwest of the orebodies (Fig. 3a). There are seven N-S-trending

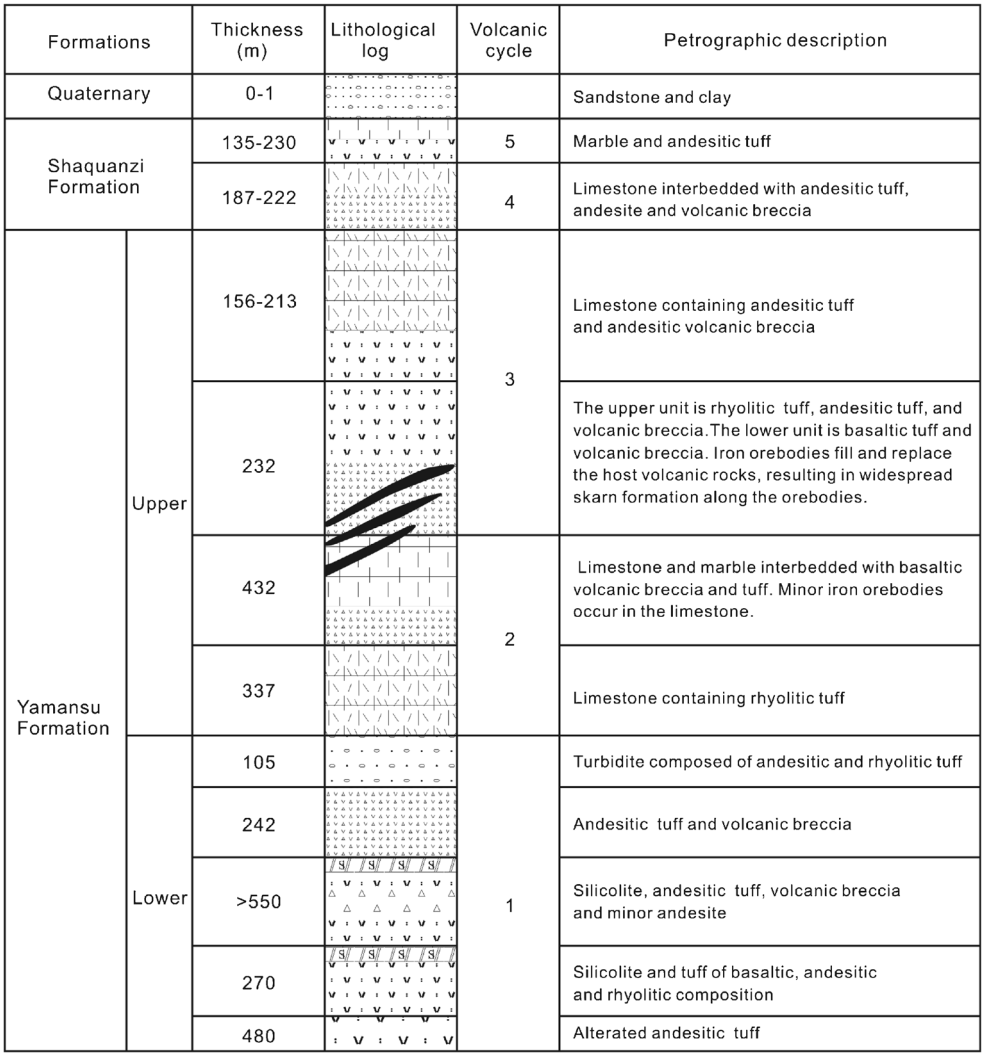

Fig. 2 Comprehensive stratigraphic column of the Yamansu ore district (modified from Zhang and Zhang 1996)

mafic dykes in the open pit of the Yamansu deposit (Li 2012). These Permian dykes are 10 to 50 cm wide and crosscut the marble and basalt (Li 2012). Minor pyrite and garnet skarn formed in the contact zone between the mafic dykes and marble (Li 2012).

Skarns

Skarns are ubiquitous and intensively developed in the Yamansu deposit. A body of skarn has a strike length of ~ 1000 m, a depth in excess of 600 m, and an average width of 120 m as revealed by drilling (Fig. 3b). This skarn body has a sharp boundary with the country rocks of marble and basalt and is closely associated with the orebodies (Online Resource 1; a, b). Limestone was partly altered with obvious alteration bands nearly parallel to the sedimentary bands (Online Resource 1; c). The skarn is commonly closely associated with ores and altered volcanic rocks (Online Resource 1; d). Relics of garnet in the massive ores (Online Resource 1; e) indicate the earlier formation of garnet skarn. The garnet skarn is mainly composed of garnet with minor diopside (Online Resource 1; e), overprinted by later hydrothermal alteration consisting of epidote, chlorite, amphibole, prehnite, and pyrite (Online Resource 1; f–h).

Iron orebodies

There are more than 16 orebodies in the deposit, constituting a mineralized belt 1640 m long and 120 m wide with an area of 0.2 km^2 (Yao et al. 1993). The orebodies are hosted in calcic skarn and locally in limestones adjacent to the skarn, occurring as EW-trending bodies with stratabound or lenticular shapes (Fig. 3a, b). They have abrupt contact with country rocks (Online Resource 1; a, b). No. 1, 2, 4, and 8 orebodies are the largest ones. No. 1 orebody is in the lower part of the iron ore belt and is > 940 m long, and dips southwards at 43° at surface to 72° at 560 m below (Yao et al. 1993). This orebody has a width of 1.25–19.3 m (Yao et al. 1993). The ore grade is 20.9–63.7% total

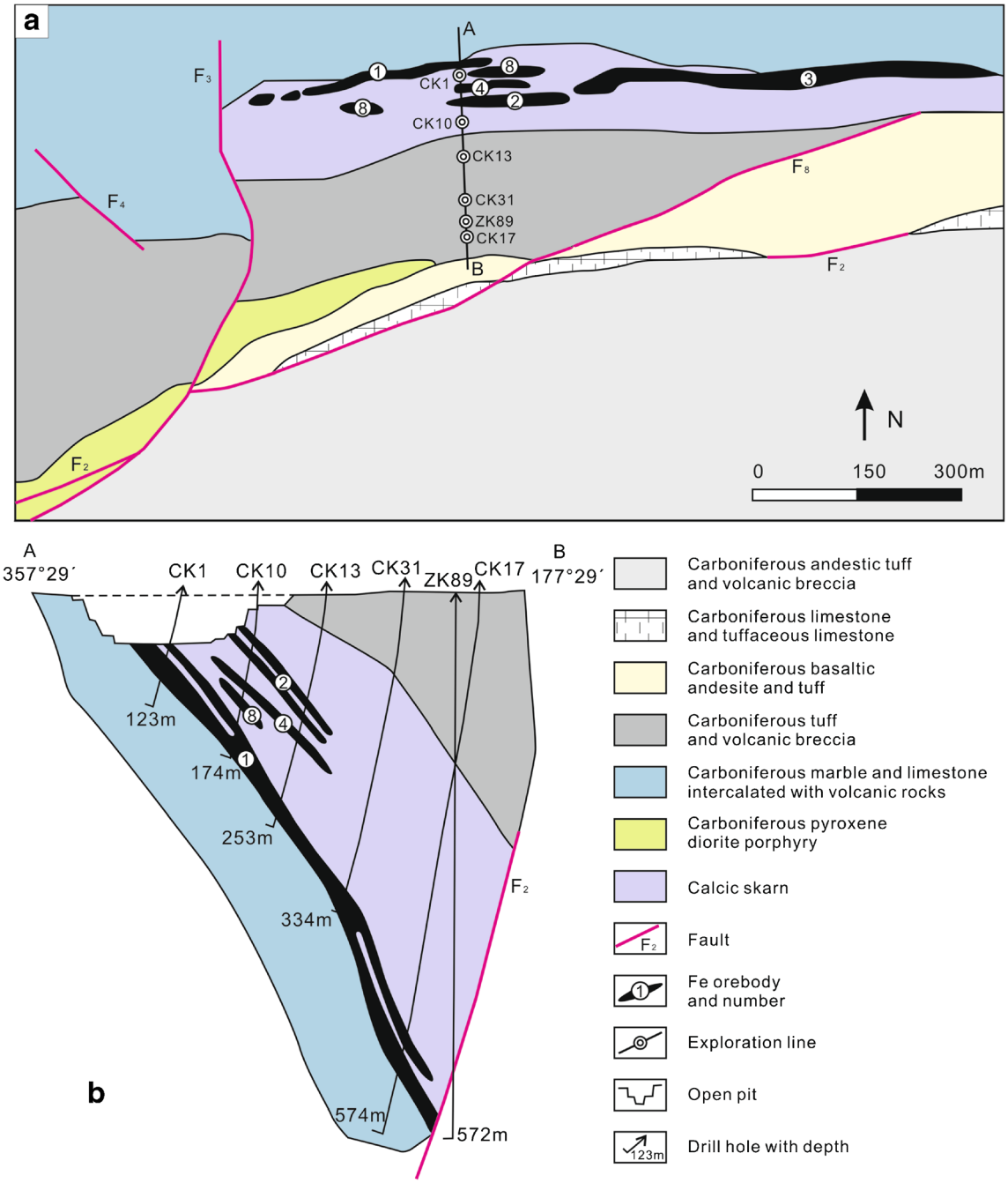

Fig. 3 Geological (**a**) and cross section (**b**) map of the Yamansu deposit (modified from Hou et al. 2014b)

Fe with an average grade of 47.7% (Yao et al. 1993). The No. 2 and 3 orebodies are located in the upper part of the ore belt and probably merge into one orebody, which dips southwards at 35–55° and has a length of 1084 m, a width of 6–62 m, and an average thickness of 17.6 m. The No. 2 + 3 orebody has a grade of 27.3–62.9% total Fe and an average grade of 54.9%. The No. 4 and 8 orebodies are located in the middle part of the ore belt. The No. 4 orebody is 108 m long and 8 m wide at the surface and dips southwards at 35–50°. The No. 8 orebody is 55 m long and 5 m wide and is 302 m at depth.

Iron-rich fragments were also identified in association with volcanic or submarine volcanic breccia and ignimbrite adjacent to the orebodies (Li et al. 2015). These fragments display typical volcanic fabric features, such as porphyritic texture, and hyalopilitic texture of the groundmass and vesicles filled by minerals to form amygdales. Iron-rich fragments are composed of mainly magnetite with various amounts of oligoclase, albite, and K-feldspar. These fragments are characterized by high Si, Al, Fe, Ca, Ti, Na, and K contents and low Mg content with the average total Fe content of 26% (Li et al.

2015). Magnetite in these fragments is mostly Ti-V-rich magnetite, with the TiO_2 content ranging up to 4.9 wt% and V_2O_3 content up to 3.2 wt% (Li et al. 2015).

Mineralization

Magnetite and pyrite are the dominant ore minerals. Chalcopyrite is not common and is commonly altered to malachite. Gangue minerals include garnet, hornblende, biotite, chlorite, epidote, quartz, calcite, and other calc-silicate minerals. Jarosite, malachite, and gypsum are supergene in origin. Ores are mainly massive and banded, but disseminated ores and ore veinlets are locally present. Massive ores commonly contain 80–90 modal% magnetite and 10–20 modal% pyrite, calcite, or garnet (Online Resource 2; a–e). Most of the massive ores are crosscut by calcite or quartz veins (Online Resource 2; a, d). Some massive ores are poorly consolidated with pores filled by pyrite and chlorite (Online Resource 2; e). Banded ores consist of 60–80 modal% magnetite and 20–40 modal% garnet and/or pyrite (Online Resource 2; f-h). Bands of magnetite range from a few millimeters to about 5 cm (Online Resource 2; f–h). The boundaries between bands are sharp (Online Resource 1; e and Online Resource 2; f) or gradational (Online Resource 2; g, h). Disseminated ores have fine-grained magnetite in skarn or wall rocks (Online Resource 2; i). Magnetite and/or hematite veins of variable width crosscut the early garnet skarn (Online Resource 2; j, k) or marble (Online Resource 2; l).

Paragenetic sequence of alteration and mineralization

Extensive alteration surrounding the orebodies includes skarn, epidote, chlorite, pyrite, carbonate, and silicate alteration from early to late. Skarn is the main alteration type closely related to iron mineralization. Based on the macro- and microtextural relationships of mineral assemblages, four principal stages of alteration and mineralization are identified in the Yamansu deposit (Fig. 4). The paragenetic sequence includes garnet-diopside (I), magnetite (II), hydrous silicate-sulfide (III), and calcite-quartz (IV) stages.

Stage I: garnet-diopside stage

This stage is dominated by garnet and diopside, similar to the typical prograde stage of skarn deposits. In most cases, garnet is more common and diopside can only be identified under the microscope. Garnet shows dark brown, red brown, and light brown colors from early to late (Online Resource 1; d, e) and has a grain size ranging from a few millimeters to centimeters (Online Resource 2; c, i, j). The different colors of garnet represent different Fe and Al contents. Electron microprobe analyses show that garnet in the Yamansu deposit belongs to the andradite-grossular series (Li 2012; Li et al. 2014). The formation temperature of garnet is 310–800 °C (Zhang and Zhang 1996). Garnet is contemporary with magnetite (Online Resource 2; c and Fig. 5a) or forms slightly earlier than magnetite (Online Resource 2; g, i, j and Fig. 5b, c). Diopside commonly occurs as radial aggregates associated with garnet (Fig. 5a). This stage is similar to the prograde stage of skarn Fe mineralization elsewhere (Meinert et al. 2005).

Stage II: magnetite stage

This is the main stage of Fe mineralization. Magnetite is the dominant ore mineral associated with garnet and diopside (Fig. 4). Magnetite occurs as massive aggregates, disseminated grains, or veins (Online Resource 2). Magnetite typically occurs as subhedral to euhedral grains ranging from 10 to 500 μm in length (Fig. 5a–d). Some magnetite grains are radial and rounded (Fig. 5b, d) and are locally replaced by hematite (Fig. 5d). Some magnetite grains show compositional zoning and are composed of dark and light domains in backscattered electron (BSE) images (Fig. 5e). Quartz and calcite associated with magnetite have fluid inclusion homogenization temperatures of 362 to 476 °C (Zhang and Zhang 1996).

Stage III: hydrous silicate-sulfide stage

This stage is characterized by the wide occurrence of pyrite, chalcopyrite, actinolite, epidote, chlorite, and prehnite (Online Resource 2; a, b, f and Fig. 6). Pyrite occurs as veins with varying width crosscutting massive ores (Online Resource 2; a, f) or occurs as massive aggregates associated with magnetite (Online Resource 2; b, g). Pyrite is also disseminated in massive and banded ores (Online Resource 2; d, e). Pyrite occurs as subhedral to euhedral grains ranging from 10 to 1000 μm in diameter (Fig. 5f–h). Chalcopyrite is rare and associated with pyrite, actinolite, and quartz (Fig. 5f, g). Part of chalcopyrite grains has been oxidized to malachite (Fig. 5h). Epidote and chlorite commonly occur as veins in massive ores (Online Resource 2; a), indicating their later formation than magnetite. Epidote and chlorite are also widespread in altered volcanic rocks (Online Resource 1; f–h). The calculated temperature for chlorite formation is about 280 °C using the chlorite geothermometer (Li 2012). This stage is similar to the retrograde stage of skarn Fe mineralization elsewhere (Meinert et al. 2005).

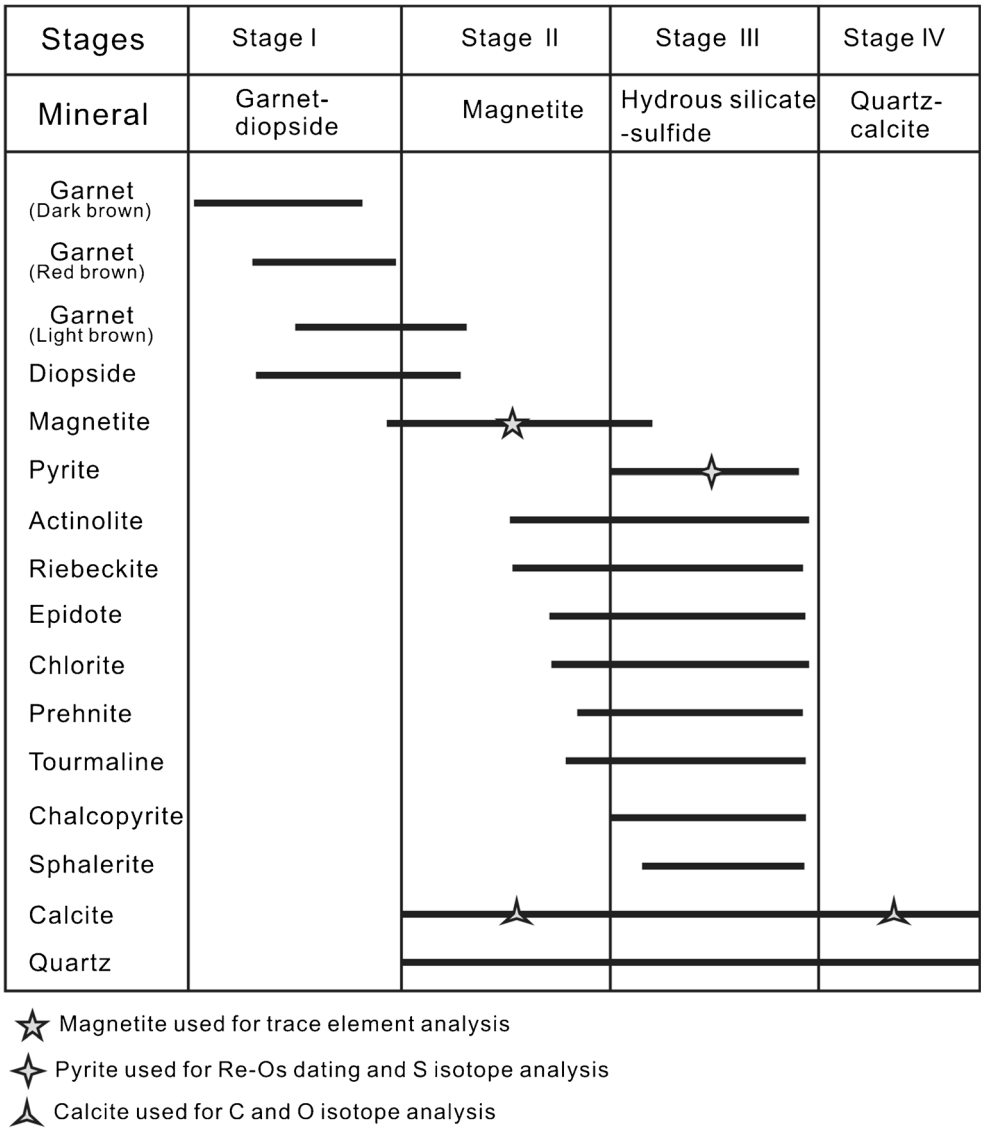

Fig. 4 Simplified paragenetic sequence of mineralization and alteration in the Yamansu deposit (modified from Li et al. 1986)

Stage IV: calcite-quartz stage

Later calcite ± quartz veins are widespread in the Yamansu deposit. Calcite ± quartz veins commonly crosscut early ores (Online Resource 2; a, d, f), indicating their later formation. The veins have the width ranging from a few millimeters to 2 cm.

Analytical methods

Re-Os isotope analyses

Eleven pyrite separates from the magnetite-sulfide ores were selected for Re-Os isotope analysis. Ores were crushed and sieved, and magnetite was removed by a magnet. Pyrite grains were separated by heavy liquid and then hand-picked under a binocular microscope. The grains range in size from 150 to 250 μm. Re and Os isotopes were analyzed using a PE ELAN DRC-e ICP-MS in the State Key Laboratory of Ore Deposit Geochemistry, Institute of Geochemistry, Chinese Academy of Sciences (IGCAS), Guiyang, China. The detailed analytical procedure was described in Qi et al. (2013). Approximately 0.05 to 0.1 g of pyrite was weighed and loaded into a 200-ml Carius tube with known amounts of ^{185}Re and ^{190}Os spikes. Samples were then digested and equilibrated using 10 ml concentrated HNO_3 and 2 ml HCl at 200 °C for about 12 h. Osmium was separated as OsO_4 from the matrix using in situ distillation equipment and Re was separated from the remaining solution after Os distillation using anion exchange resin (Biorad AG 1 × 8, 200–400 mesh) (Qi et al. 2007; Qi et al. 2010). Iridium was added to Re and Os solutions for mass discrimination correction (Schoenberg et al. 2000; Huang et al. 2013b). Procedural blanks were 7.0 ± 1.0 pg ($n = 2$)

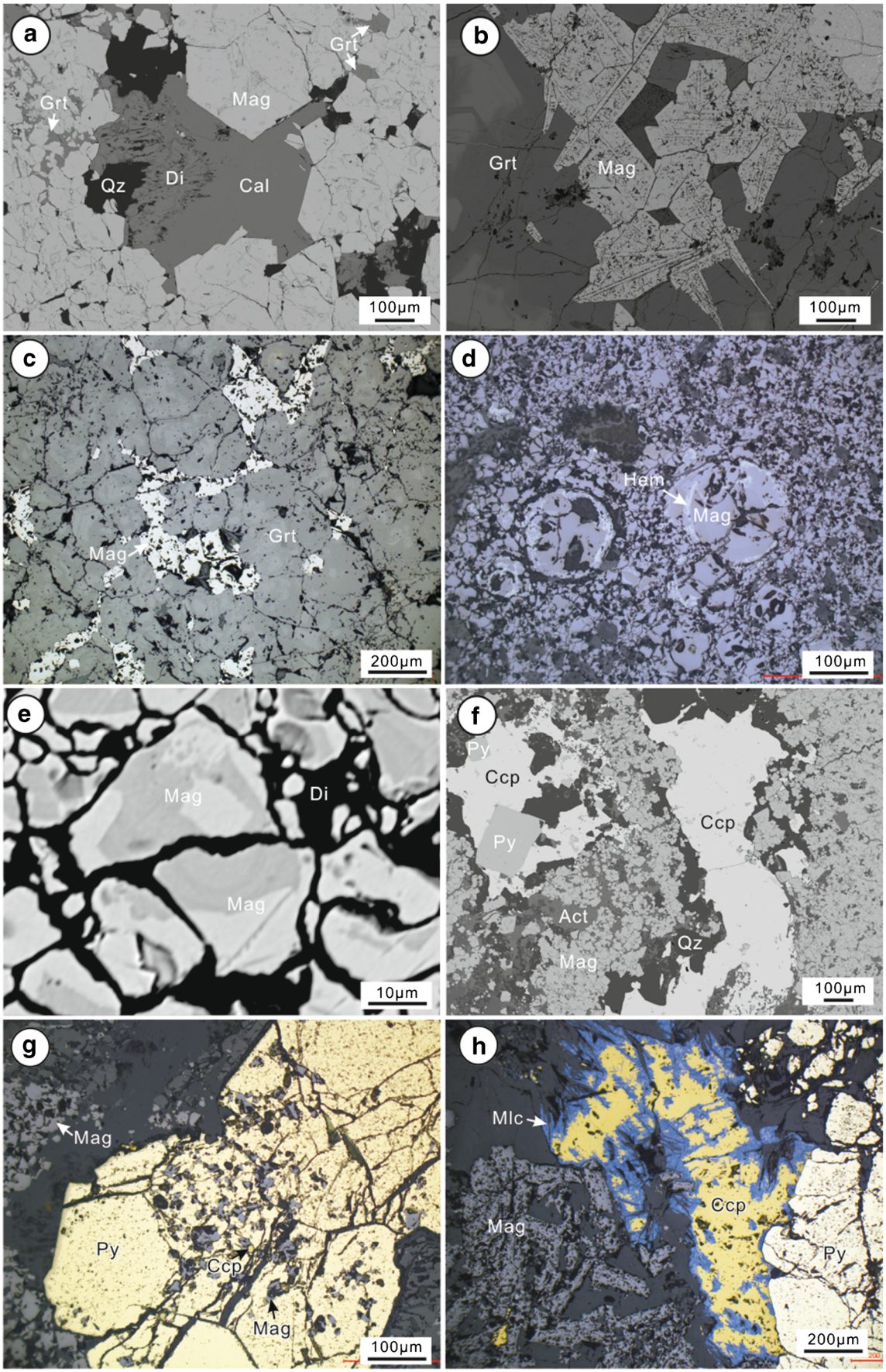
a
Grt
Grt
Mag
Qz
Di
Cal
100μm
b
Grt
Mag
100μm
c
Mag
Grt
200μm
d
Hem
Mag
100μm
e
Mag
Di
Mag
10μm
f
Py
Ccp
Py
Ccp
Act
Qz
Mag
100μm
g
Mag
Py
Ccp
Mag
100μm
h
Mlc
Ccp
Mag
Py
200μm

◀ **Fig. 5** Photomicrographs of ores in the Yamansu deposit. **a** Euhedral magnetite associated with garnet, calcite, quartz, and diopside (BSE image). **b** Needle-like or foliaceous magnetite associated with zoned garnet (BSE image). **c** Subhedral to anhedral magnetite between euhedral zoned garnets indicates the later formation of magnetite. **d** Circular coarse-grained magnetite surrounded by anhedral fine-grained magnetite. Magnetite partly replaced by hematite. **e** Single magnetite grain composed of dark and light domains (BSE image). **f** Fine-grained magnetite associated with pyrite, chalcopyrite, actinolite, and quartz (BSE image). **g** Fine-grained magnetite replaced by pyrite and chalcopyrite. **h** Chalcopyrite partly oxidized to malachite along the grain margin. Mineral abbreviations: *Act* actinolite, *Cal* calcite, *Ccp* chalcopyrite, *Chl* chlorite, *Di* diopside, *Ep* epidote, *Grt* garnet, *Hem* hematite, *Mag* magnetite, *Mal* malachite, *Py* pyrite, *Qz* quartz

and 1.5 ± 0.1 pg ($n = 2$) for Re and Os, respectively, with an average $^{187}Os/^{188}Os$ value of 0.55 ± 0.10 (1σ, $n = 2$). Absolute uncertainties (2σ) are derived from error propagation of uncertainties in Re and Os mass spectrometer measurements, blank abundances and isotopic compositions, and spike calibrations.

Stable isotope analyses

Sulfur isotopes were analyzed using a EuroVector EA3000 element analyzer (EA) coupled to a GV IsoPrime IRMS (EA-IRMS) at the State Key Laboratory of Environmental Geochemistry, IGCAS. The method was similar to that described in Huang et al. (2013b). The sulfur isotopic compositions are reported as δ-notation in per mil (‰) relative to Vienna-Canyon Diablo Troilite (VCDT). Replicate analyses of Chinese Ag_2S standard GBW04415 yielded $\delta^{34}S$ values of 22.13 ± 0.08‰ (1σ, $n = 12$), in good agreement with the certified values of 22.15 ± 0.14‰ (1σ) (Ding et al. 2001).

Carbon and oxygen isotopic compositions were determined at the State Key Laboratory of Ore Deposit Geochemistry, IGCAS, using a GasBench II device in the continuous flow mode coupled with a MAT 253 Isotope Ratio Mass Spectrometer (IRMS) following the equilibration method (Rangarajan and Ghosh 2011). The carbon dioxide gas was extracted by reaction with 15 drops of pure phosphoric acid in a sealed quartz tube at 72 °C for 1 h and carried to a mass spectrometer by helium gas. Carbon and oxygen isotope ratios afforded by IRMS are expressed as δ-notation in per mil (‰) relative to Vienna-Pee Dee Belemnite (VPDB). The oxygen isotope ratios are usually reported to be relative to Vienna-Standard Mean Ocean Water (VSMOW) standard. Duplicate analyses of standards have a precision better than 0.2‰.

Electron probe microanalyses

Major and selected trace elements in magnetite were measured using a JEOL JXA-8230 Electron Probe Micro-Analyzer (EPMA) at the Testing Center of Shandong Bureau of China

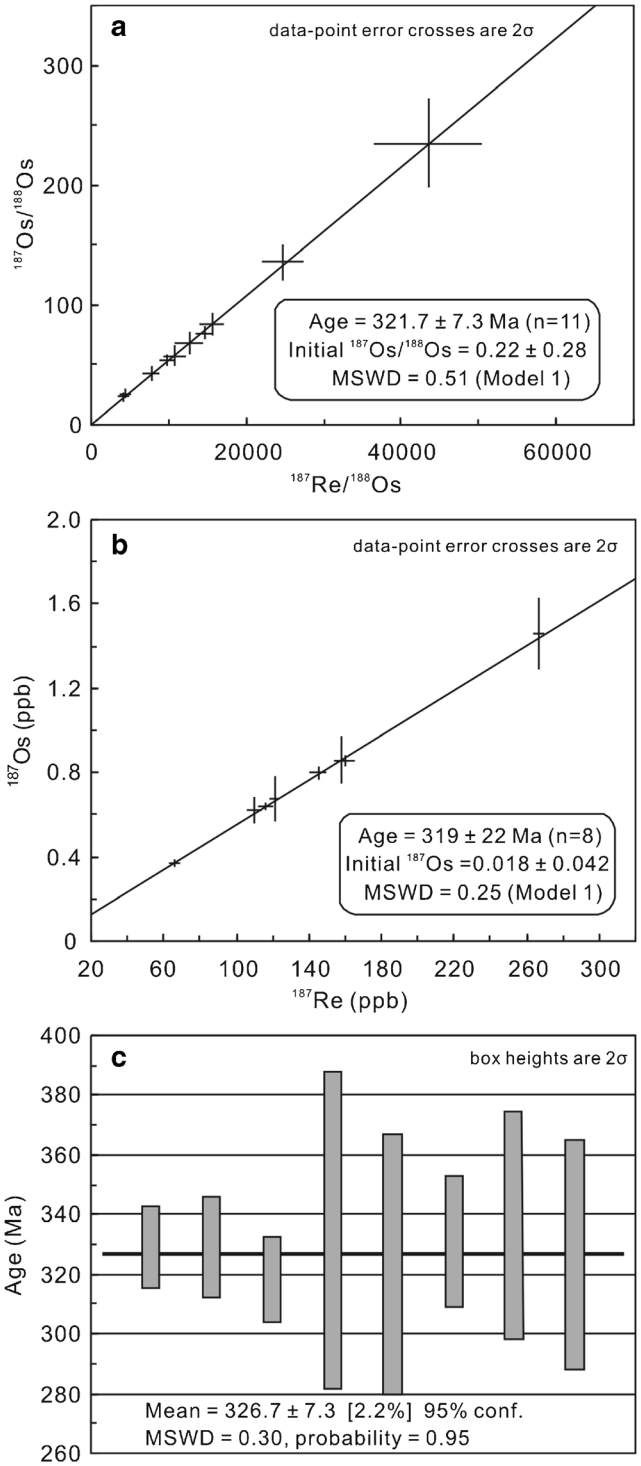

Fig. 6 **a** Plot of $^{187}Re/^{188}Os$ versus $^{187}Os/^{188}Os$ for all pyrite samples. **b** Plot of ^{187}Re versus ^{187}Os for LLHR pyrite. **c** Weighted average of Re-Os model ages for LLHR pyrite. Regression of all data was performed using Isoplot version 3.27 (Ludwig 2003). Error correlation coefficient (rho) was added during regression of isotope ratios. *MSWD* mean square of weighted deviate

Metallurgical Geology Bureau, Jinan, China. Elements were analyzed using an accelerating voltage of 15 kV, a beam current of 20 nA, and a beam spot of 1 μm. Matrix effects were

corrected using the ZAF software provided by JEOL. The accuracy of the reported values for the analyses is 1–5% depending on the abundance of the element. The detailed operating conditions and mean detection limits of elements are listed in Online Resource 3. In addition to quantitative spot analyses, wavelength dispersive X-ray (WDX) maps were collected using an accelerating voltage of 20 kV, a probe current of 100 nA, point size of 0.3 × 0.3 μm, and dwell time of 5 ms for acquisition on each point.

Laser ablation ICP-MS trace element analyses

Thin sections of ore samples were examined by electron microprobe to characterize the textures of magnetite prior to LA-ICP-MS analysis. Major and trace elements of magnetite were determined by a Coherent GeoLasPro 193 nm laser ablation system coupled with an Agilent 7700x ICP-MS at the State Key Laboratory of Ore Deposit Geochemistry, IGCAS. Helium was applied as a carrier gas and argon was used as the make-up gas and mixed with the carrier gas via a T-connector before entering the ICP. Each analysis includes a background acquisition of approximately 20 s (gas blank) followed by 40 s data acquisition from the sample. Analytical spots (32 μm) were ablated by 160 successive laser pulses (4 Hz). Every 8 sample analyses were followed by one analysis of GSE-1G as quality control to correct the time-dependent drift of sensitivity and mass discrimination. A komatiitic glass (GOR-128g) and a natural magnetite (BC28) from the Bushveld Complex were also used to monitor the data quality by analyzing it as an unknown sample each run. Off-line selection and integration of background and analyte signals, and time-drift correction and quantitative calibration were performed by ICPMSDataCal (Liu et al. 2008). Element contents were calibrated against multiple reference materials (GSE-1G, BCR-2G, BIR-1G, BHVO-2G, and NIST 610) using ^{57}Fe as internal standard (Liu et al. 2008; Gao et al. 2013). The analytical results of monitoring samples BC28 and GOR-128g are consistent with their certified values and reported values from previous studies (Online Resource 3).

Results

Re-Os isotope composition

The Re-Os isotope composition of pyrite samples is listed in Online Resource 4. Pyrite has total Re and Os contents ranging from 105 to 426 ppb and from 0.432 to 1.193 ppb, respectively (Online Resource 4). Pyrite has small amounts of common Os contents of 0.026–0.776 ppb (Online Resource 4). As a result, they have highly variable $^{187}Re/^{188}Os$ and $^{187}Os/^{188}Os$ values of 669–43,479 and 3.8–235, respectively. Due to low common Os, the blank ^{188}Os accounts for a significant component of the measured value, which would result in highly correlated uncertainties between $^{187}Re/^{188}Os$ and $^{187}Os/^{188}Os$ values. To correct this effect, the $^{187}Re/^{188}Os$ and $^{187}Os/^{188}Os$ data are plotted with the associated uncertainty correlation value (rho; 0.29–0.96) (Ludwig 1980) and 2σ uncertainties. Conventional plot of $^{187}Re/^{188}Os$ versus $^{187}Os/^{188}Os$ regression analysis for all pyrite samples yields a model 1 isochron age of 321.7 ± 7.3 Ma and an initial $^{187}Os/^{188}Os$ value of 0.22 ± 0.28 (2σ, MSWD = 0.51, Fig. 6a). The ^{187}Os budget is predominately composed of radiogenic ^{187}Os ($^{187}Os^r$; 94.3–99.9%) and, therefore, defines these minerals as low-level highly radiogenic (LLHR) sulfides (Stein et al. 2000). For LLHR sulfides, a direct plot of ^{187}Re and ^{187}Os contents is preferred. Regression of eight Re-Os analyses with $^{187}Re/^{188}Os$ values larger than 5000 yields a model 1 isochron age of 319 ± 22 Ma, with the initial ^{187}Os content of 0.018 ± 0.042 ppb (2σ, MSWD = 0.25; Fig. 6b). For LLHR sulfides, model ages can be calculated using ^{187}Re and $^{187}Os^r$ contents. Re-Os model ages of these pyrite samples range from 319 to 337 Ma (Online Resource 4), and the weighted average of these model ages is 326.7 ± 7.3 Ma (2σ, MSWD = 0.30, probability = 0.95; Fig. 6c), consistent with the isochron age within errors.

Sulfur isotope composition

Pyrite has $\delta^{34}S_{VCDT}$ values ranging from − 2.2 to + 2.9‰, but mostly between − 1 and 0‰ (Online Resource 4 and Fig. 7). The sulfur isotope composition of H_2S in equilibrium with pyrite can be calculated from the $\delta^{34}S_{VCDT}$ values of pyrite, appropriate fractionation factors between aqueous sulfur species and sulfide minerals, which are closely related to temperature and fO_2 during sulfide precipitation (Ohmoto and Rye 1979). Fluid inclusion homogenization temperatures of calcite associated with pyrite from this stage range from 240 to 380 °C (Zhang and

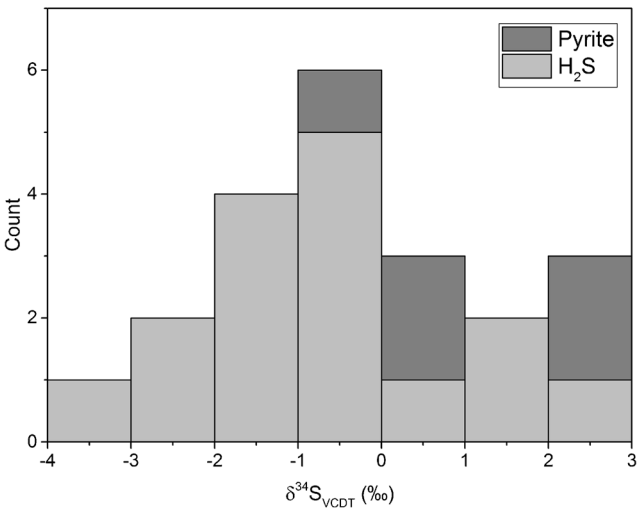

Fig. 7 Histograms showing sulfur isotope composition of pyrite from the Yamansu deposit and H_2S in fluids in equilibrium with pyrite

Zhang 1996). The sulfur isotope composition of pyrite can represent the sulfur composition of total sulfur in the hydrothermal fluids because of lack of coexisting sulfates (Kajiwara 1971). The calculated sulfur isotope composition of H_2S has $\delta^{34}S_{VCDT}$ values ranging from −3.1 to +2‰ with an average of −0.8‰ (Online Resource 4).

Carbon and oxygen isotope composition

Calcite from stage II has $\delta^{13}C_{VPDB}$ and $\delta^{18}O_{VSMOW}$ values of −2.5 to −1.2‰ and 11.8 to 12.0‰, respectively, whereas those from stage IV have values of −1.1 to 1.1‰ and −7.7 to −5.2‰, respectively (Online Resource 4). The CO_2 in equilibrium with stage II calcite has C and O isotope composition of −1.1 to 0.2‰ and 11.7 to 11.9‰, respectively, whereas CO_2 in equilibrium with stage IV calcite has these values of −4.4 to −2.2‰ and −22.2 to −19.7‰, respectively. In the plot of $\delta^{13}C_{VPDB}$ versus $\delta^{18}O_{VSMOW}$, calcite from stage II lies in the field of primary magmatic carbonate, similar to other Fe deposits in the same belt (Fig. 8a). Carbon in stages II and IV has an isotope composition close to mantle CO_2 (Fig. 8b). Stage II fluids have O isotope composition slightly higher than magmatic water, close to metamorphic and formation water compositions, whereas stage IV fluids have O isotope composition typical of admixture of meteoric water (Fig. 8c).

Chemical zoning of magnetite

In the Yamansu deposit, some magnetite grains have two main domains under BSE imaging (Figs. 5e and 9). One domain is dark and smooth, whereas the other domain is light and sometimes porous (Fig. 9). Light and dark domains in the same magnetite grain can form obviously oscillatory zoning or sector zoning (Fig. 9a, b). Dark domains can be replaced to various extent by light domains along fractures and/or grain boundaries that have appreciable porosities (Fig. 9c, d), whereas light domains are generally in sharp contact with dark domains and contain numerous solid inclusions such as carbonate and silicate minerals (Fig. 9c). Single

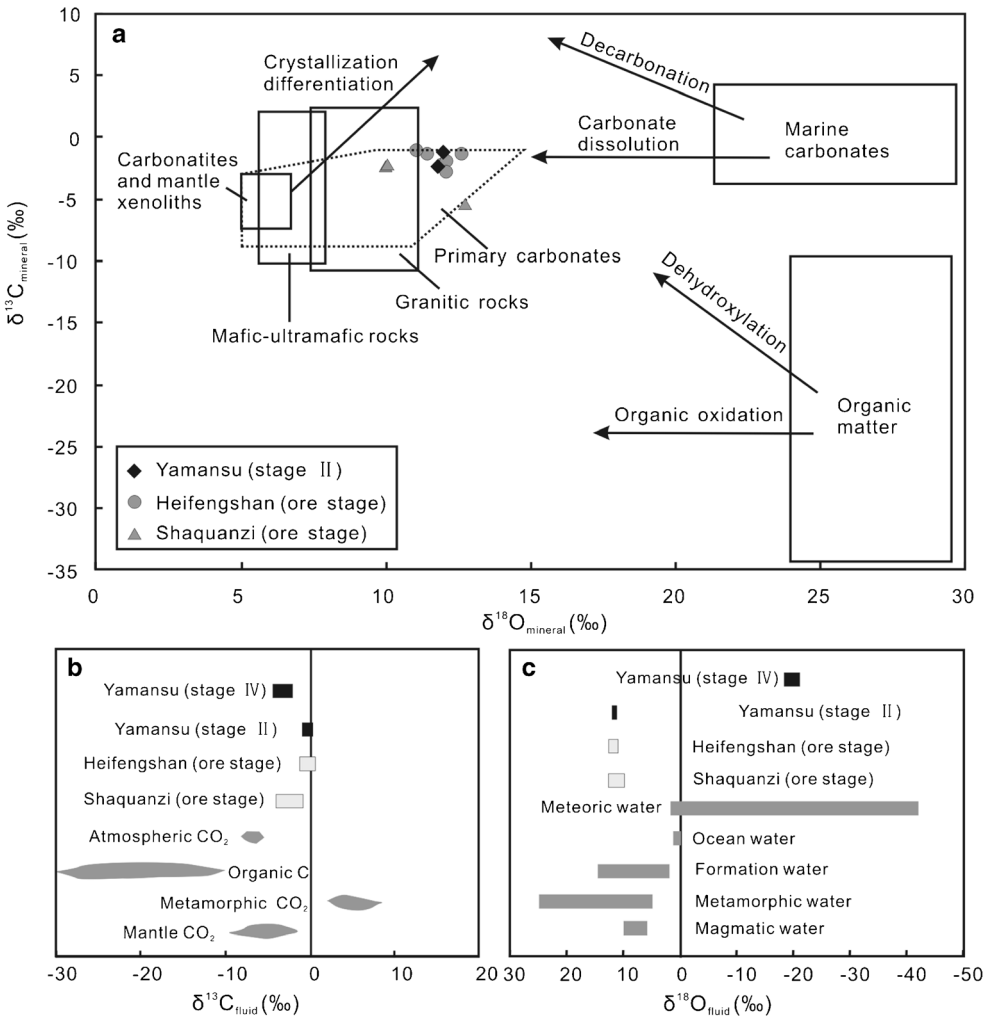

Fig. 8 **a** $\delta^{13}C_{PDB}$-$\delta^{18}O_{SMOW}$ diagram of calcite from the Yamansu Fe deposit. Data sources: mantle-derived rocks, granitic rocks, primary carbonates, marine carbonates, and sedimentary organic carbon (Ohmoto 1986; Valley 1986; Nelson et al. 1988; Hoefs 1997; Ray et al. 1999). **b**, **c** $\delta^{13}C_{PDB}$ (after Clark and Fritz 1997) and $\delta^{18}O_{SMOW}$ (after Hoefs 1997) values of calcite and representative geological reservoirs. Calcite from the Heifengshan Fe deposit and Shaquanzi Fe-Cu deposit in the same belt with the Yamansu deposit are also shown for comparison (Huang et al. 2013a)

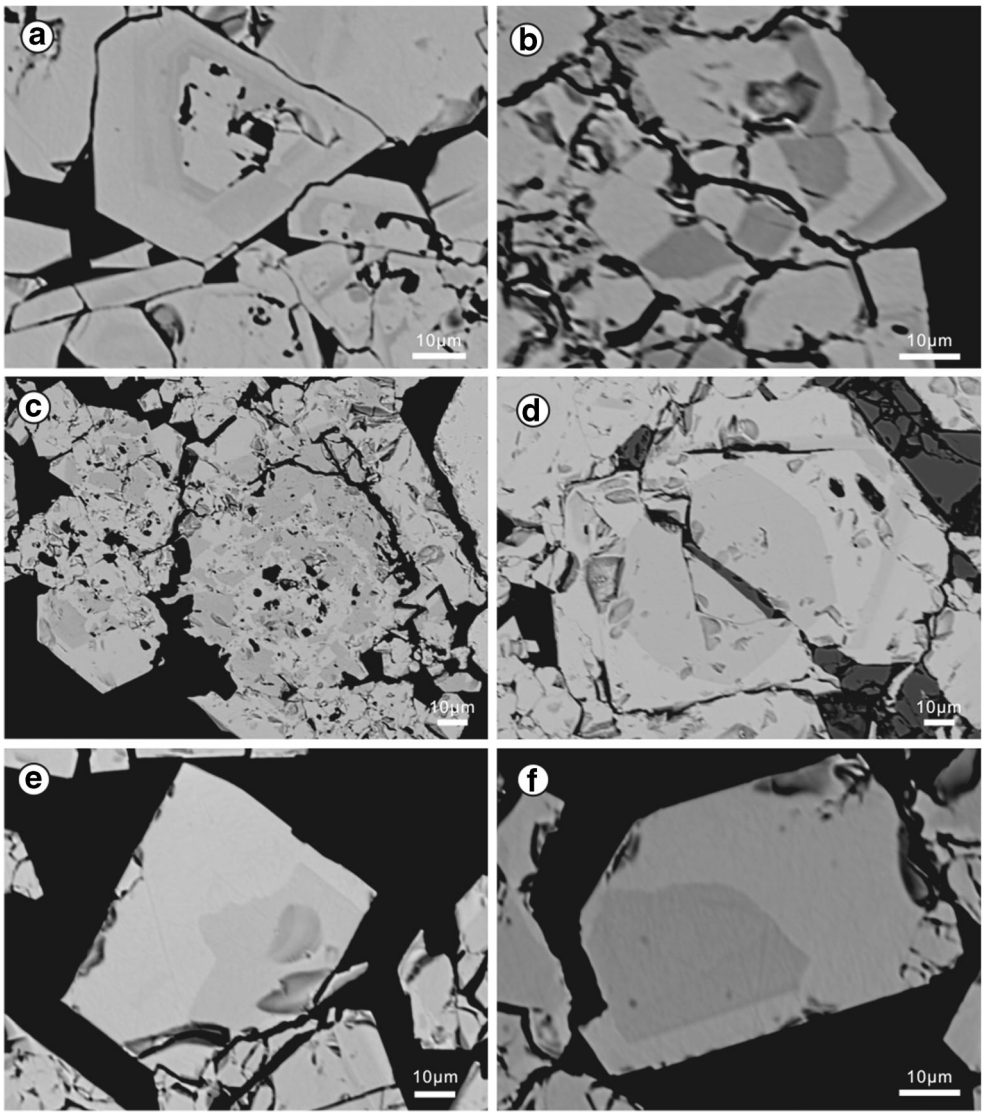

Fig. 9 BSE images showing microtextures of magnetite. **a** Euhedral zoned magnetite composed of dark and light domains. The dark domains show obvious oscillatory zoning. **b** Subhedral magnetite grains composed of light and dark domains, forming zoned magnetite with sector zoning. **c** Subhedral to anhedral magnetite grains composed of early dark and late light domains. Light domains are porous. **d** Subhedral magnetite grains composed of light domain in the rim and dark domain in the center. **e**, **f** Euhedral magnetite grain composed of light and dark domains

magnetite grains may show obvious compositional zoning of dark and light domains (Fig. 9e, f). EPMA mapping shows that light magnetite has higher Fe content but lower Al, Si, and Mg contents than dark magnetite (Fig. 10). Quantitative analyses of 46 spots indicate that light magnetite has higher Cr but lower Mn, Ca, and Ti contents than dark magnetite (Online Resource 4 and Fig. 11a). Due to different Ca+Al+Mn and Ti+V contents, light and dark magnetite domains define different populations (Fig. 11b).

LA-ICP-MS trace element compositions of magnetite

Due to the small scale zoning, light and dark domains cannot be separated during laser ablation, and thus, the LA-ICP-MS results represent the mixed composition of light and dark domains. In this study, only magnetite grains without zoned textures are analyzed. One hundred and twenty-nine analyses were obtained. The average values and standard deviations of trace element contents of magnetite are listed in Online Resource 4. Full analytical results of LA-ICP-MS for different groups of magnetite are presented in Online Resource 5. Forty-seven elements were analyzed but only 28 elements were detected. Elements, such as Sc, P, Ge, Nb, Hf, Ta, Ag, Cd, In, and Au, are below the detection limits. Some magnetite grains also have Cr, Ni, Cu, As, Rb, Y, Zr, Mo, Sn, Sb, Ba, W, Bi, and Th contents lower than the detection limits.

Most element contents vary within one or two orders of magnitude, but some elements such as V, Y, Mo, W, Pb, and U vary up to three or four orders of magnitude (Fig. 12). Most magnetite grains have Mg, Al, Si, Ca, Ti, and Mn contents between ~ 100 and 10,000 ppm; V, Cr, Co, Ni, Zn, Ga, and As contents between ~ 1 and 100 ppm; and Y, Zr, Mo, Sn, Sb, Bi, Th, and U contents lower than

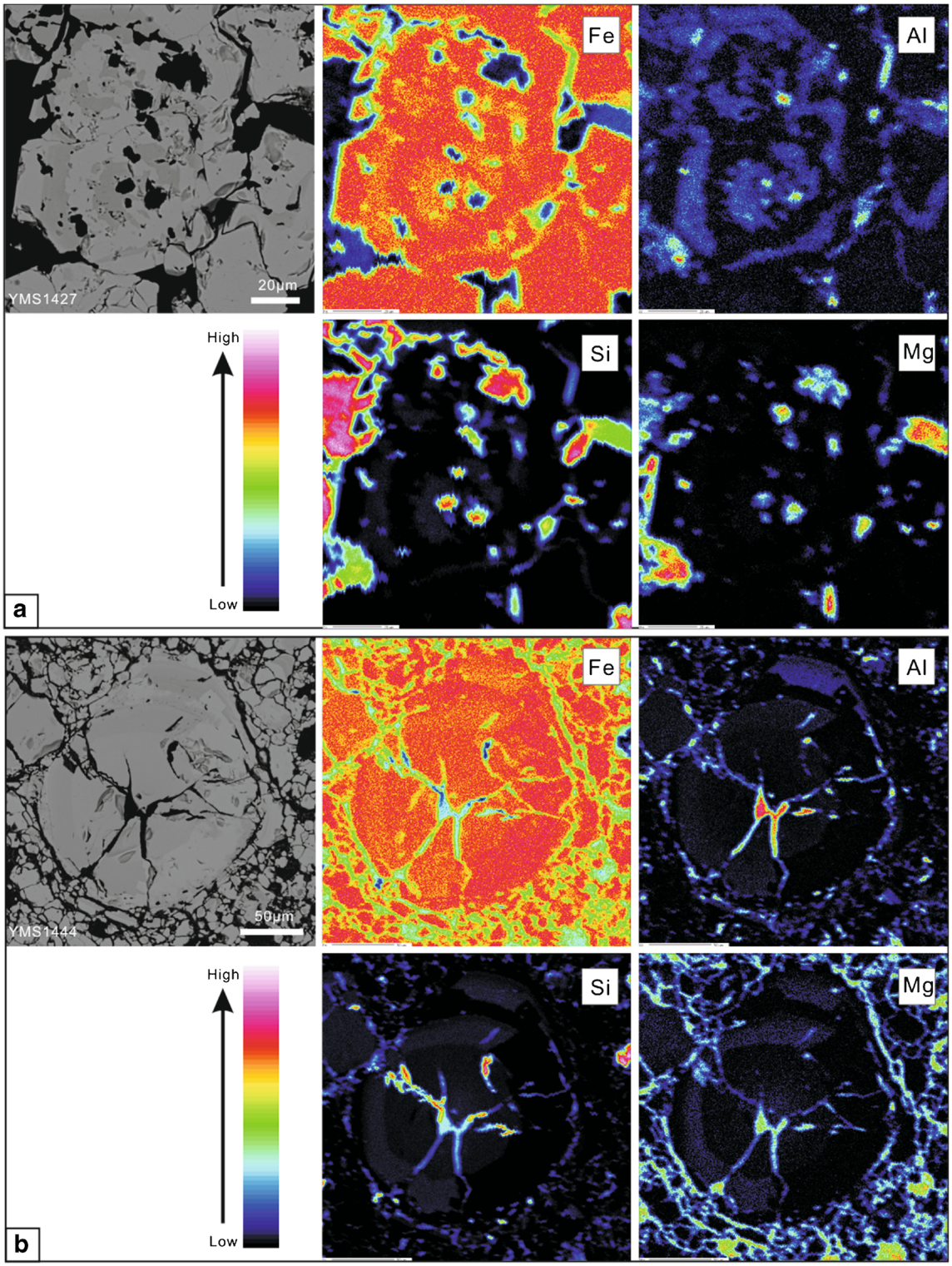

Fig. 10 **a**, **b** BSE images of magnetite grains and corresponding wavelength dispersive X-ray maps of selected trace elements in magnetite from the Yamansu deposit. The dark and light domains of magnetite grains have different Fe, Al, Si, and Mg contents

10 ppm (Fig. 12). Several elements show good correlation. Aluminum shows positive correlations with Mg, Mn, and Ga (Fig. 13a–c). There are also positive correlations of Si with Ca and Mg (Fig. 13d, e). Antimony shows positive correlations with As and Bi (Fig. 13f, g). Tungsten shows a positive correlation with Mo (Fig. 13h).

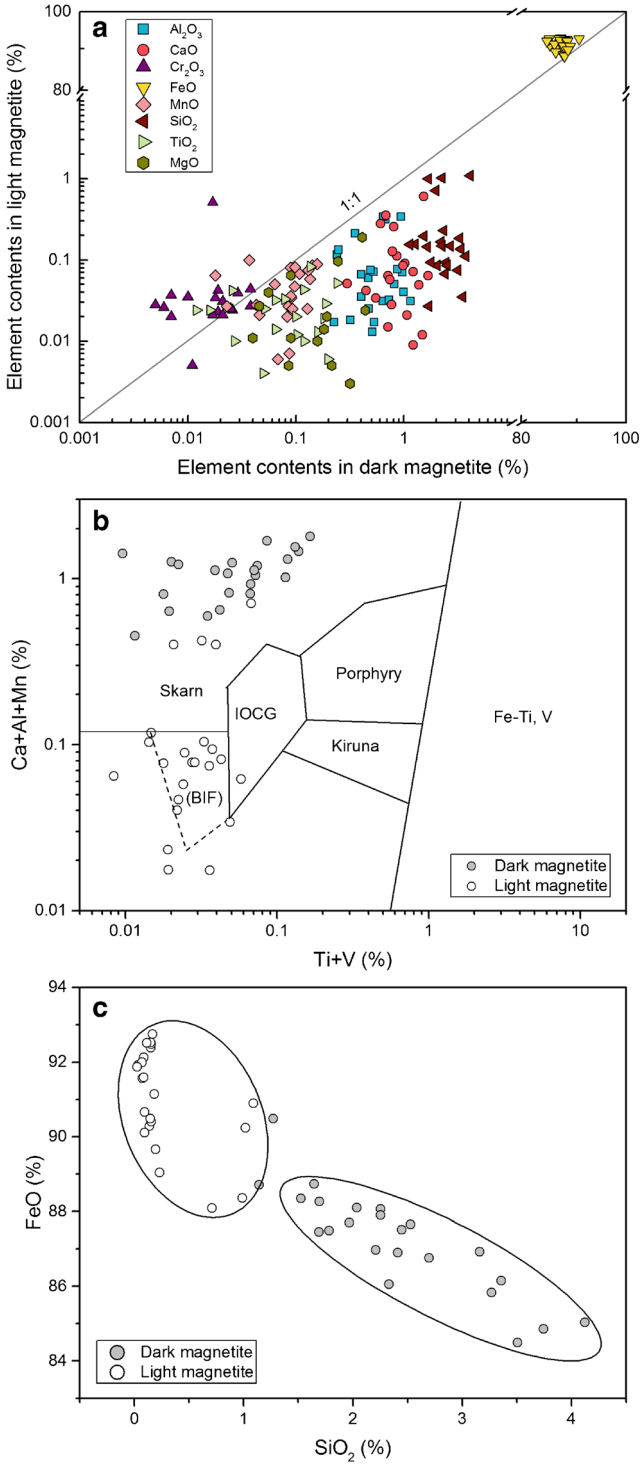

Fig. 11 **a** Binary plots showing EPMA data of dark magnetite and light magnetite. Dark magnetite has lower Fe and Cr contents but higher Al, Si, Mg, Mn, Ti, and Ca contents than light magnetite. **b** Plot of Ca+Al+Mn versus Ti+V showing skarn-like dark magnetite. **c** Plot of FeO versus SiO_2 showing varying compositions between dark magnetite and light magnetite. Data points are individual analyses. Reference fields are from Dupuis and Beaudoin (2011). *BIF* banded iron formation, *Skarn* Fe-Cu skarn deposits, *IOCG* iron oxide-copper-gold deposits, *Porphyry* porphyry Cu deposits, *Kiruna* Kiruna apatite-magnetite deposits, *Fe-Ti, V* magmatic Fe-Ti-oxide deposits

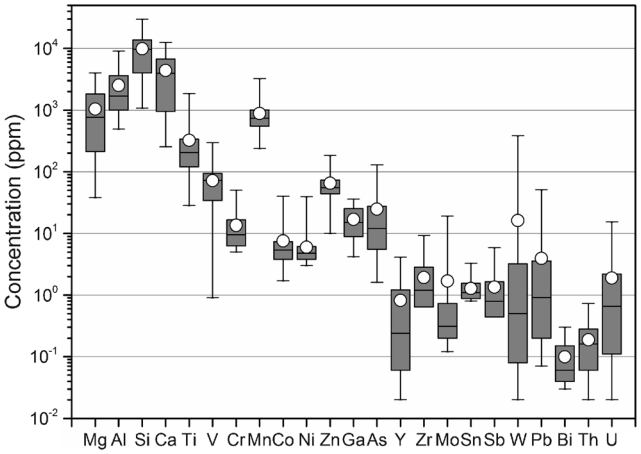

Fig. 12 Box and whisker plot for LA-ICP-MS data of magnetite grains without zoned textures. Boxes outline the 25th to 75th percentiles and whiskers extend to the minimum and maximum values. The whisker represents the range of trace element contents. The short line in the box represents the median value, whereas the circle filled white means the average value. Trace element contents below the limit of detection were removed from the box and whisker plot

Discussion

Timing of iron mineralization

Li and Chen (2003) reported a Rb-Sr isochron age of 374 ± 44 Ma for andesitic porphyry and a garnet-epidote Sm-Nd isochron age of 352 ± 46 Ma, which were thought to represent the timing of volcanism and iron mineralization, respectively. However, these ages have large errors. Hou et al. (2014b) reported a LA-ICP-MS U-Pb age of 323.5 ± 1.0 Ma for hydrothermal zircon in the skarn, which was interpreted as the age of iron mineralization.

Magnetite is the main ore mineral in Fe deposits, and thus, Re-Os dating of magnetite can provide a direct mineralization age (e.g., Mathur et al. 2002; Davies 2010; Huang et al. 2014b; Barra et al. 2017). However, magnetite in Yamansu ores has Re contents commonly lower than 1 ppb (unpublished data), which make it difficult to date magnetite using the Re-Os isotope method. Alternatively, the Re-Os isotope system of pyrite has been proved to be a reliable tool to date magmatic-hydrothermal events due to the relatively high Re in pyrite and the high closure temperature of this isotope system (Brenan et al. 2000; Morelli et al. 2004; Selby et al. 2009; Huang et al. 2013a, c). In order to obtain geologically meaningful ages, the occurrence and the paragenetic sequence of pyrite should be clearly understood. Pyrite for our Re-Os isotope analyses is closely associated with magnetite and formed simultaneously with magnetite or slightly after according to ore textures (Online Resource 2). Moreover, previous studies showed that Re-Os dating of pyrite and associated magnetite from the Shaquanzi magmatic-hydrothermal Fe-Cu deposit in the ETOB yielded similar age and demonstrated that the age of pyrite can represent the timing of iron

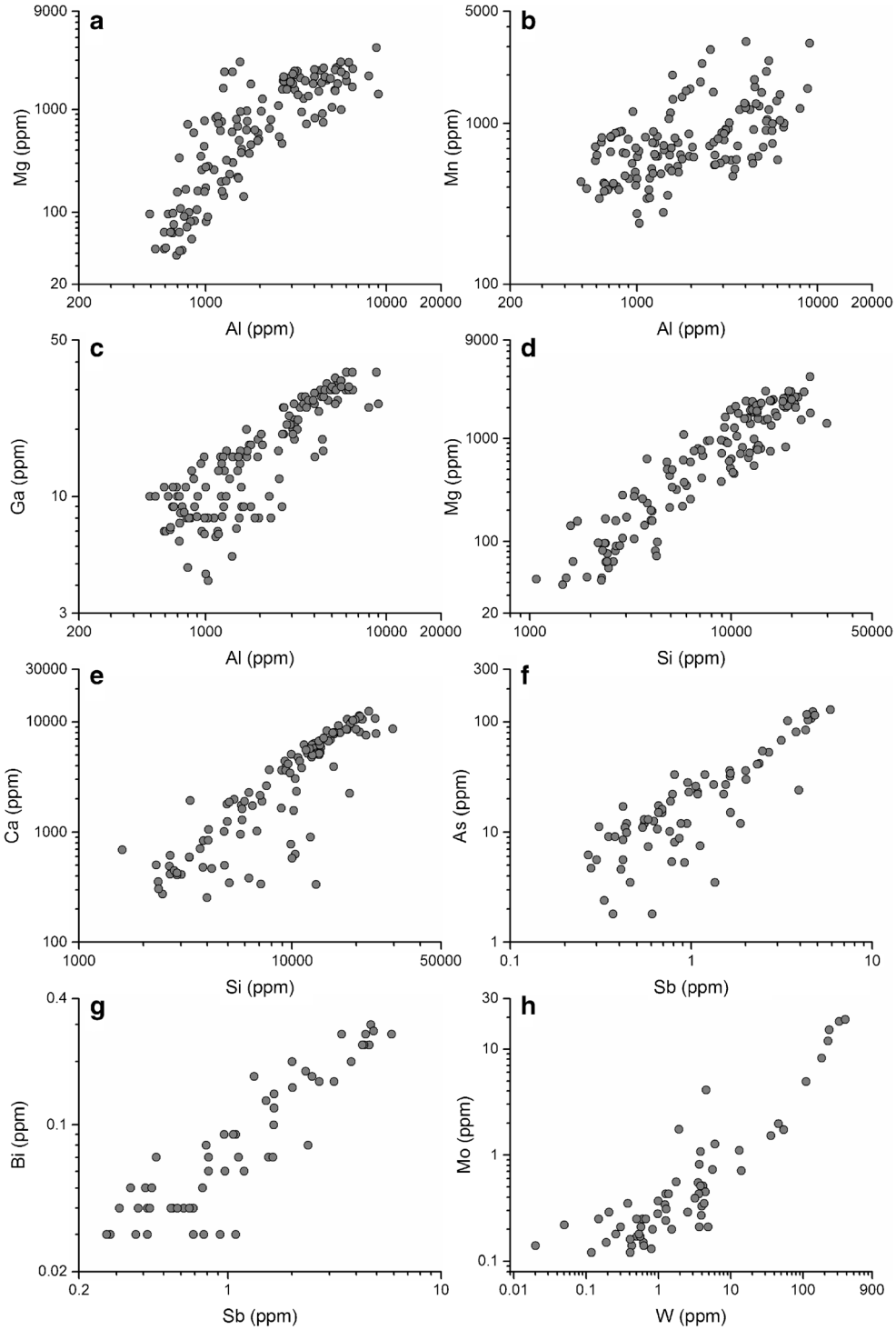

Fig. 13 Scattergrams for a selection of trace elements in magnetite without zoned textures. **a**–**c** Aluminum correlates positively with Mg, Mn, and Ga. **d**, **e** Silicon shows positive correlations with Mg and Ca. **f**, **g** Antimony shows positive correlations with As and Bi. **h** Tungsten shows a positive correlation with Mo

mineralization (Huang et al. 2014b). Pyrite separates from the Yamansu ores have a Re-Os isochron age of 321.7 ± 7.3 Ma (Fig. 6a), which represents the age of magnetite formation. Therefore, we suggest that the Yamansu deposit formed in the Early Carboniferous.

Formation of chemical zoning in magnetite

In the Yamansu deposit, the chemical zoning of magnetite is commonly composed of two types of magnetite. The dark magnetite is inclusion-free and has darker BSE contrast,

whereas the light magnetite is sometimes porous and has lighter BSE contrast (Fig. 9). Some magnetite grains exhibit obvious oscillatory zoning composed of light and dark bands of varying width (Fig. 9a, b), similar to magnetite from the Ocna de Fier-Dognecea Fe-Cu-Pb-Zn skarn deposit in Romania (Ciobanu and Cook 2004), the Fe skarn of Vegas Peledas in Argentina (Dare et al. 2014), the lava flows of EI Laco in Chile (Dare et al. 2015), and the brecciated diorite intrusion in the Los Colorados iron oxide-apatite deposit of Chile (Knipping et al. 2015b). The oscillatory zoning in magnetite is commonly interpreted as growth zoning forming as a result of changes in fluid compositions and/or physicochemical parameters (such as temperature and oxygen fugacity) during crystal growth, which periodically affect the partitioning behavior of trace elements into magnetite and co-forming minerals (Shimazaki 1998; Ciobanu and Cook 2004; Dare et al. 2015; Knipping et al. 2015b; Makvandi et al. 2015). Therefore, oscillatory zoning in zoned magnetite from the Yamansu deposit was likely derived from a fluctuating fluid composition and/or physicochemical conditions.

In addition to zoned magnetite, some magnetite also shows irregular compositional domains that include early dark Si-rich domain and late light Si-poor domain (Fig. 9c–f), which are very common in Fe skarn deposits (Ciobanu and Cook 2004; Hu et al. 2014, 2015; Zheng et al. 2017), iron oxide-apatite (IOA) deposits (Nold et al. 2014; Knipping et al. 2015a, b), and volcanogenic massive sulfide (VMS) deposits (Westendorp et al. 1991; Makvandi et al. 2016). Si-rich domains of magnetite grains have higher Mg, Al, Ca, Mn, and Ti contents, but lower Fe and Cr contents than Si-poor domains (Figs. 10 and 11). Knipping et al. (2015a, b) showed that magnetite from the Los Colorados IOA deposit (Chile) has a Ti-rich core, magmatic in origin, and a Ti-poor rim formed as a result of hydrothermal alteration of magmatic magnetite. Makvandi et al. (2016) interpreted the Si-free core of magnetite from the West Ansil bimodal-mafic VMS deposit in Quebec (Canada), as likely formed during replacement of massive sulfides by magnetite, whereas the Si-rich rim could be either the consequence of the replacement of pre-existing quartz in the massive pyrrhotite ore, or the signature of Si-rich fluids. Zheng et al. (2017) considered that the compositional variations of zoned magnetite (Ca-Si-rich rim and Ti-rich core) from the Cihai Fe skarn deposit in Xinjiang (China) resulted from the changes of fluid temperature and salinity that affected the solubility of Fe and Ti.

Dissolution-precipitation processes are commonly proposed to explain the chemical variations of different generations/types of magnetite (Putnis 2009; Putnis and John 2010; Dare et al. 2015; Hu et al. 2015; Heidarian et al. 2016). The dark magnetite has relatively higher contents of Si, Al, Ca, and Mg, which might be related to a major contribution of magmatic-derived fluids due to a large fluid-rock ratio at the site of mineral deposition (Nadoll et al. 2012, 2014; Dare et al. 2014). The dark magnetite was then extensively replaced by light magnetite preferentially along microfractures within or along grain margins (Fig. 9c, d). The replacement reactions were facilitated by a fluid-assisted process with dissolution of early magnetite and precipitation of a secondary variety near the reaction front, with Si, Al, Ca, Mg, Mn, and Ti being significantly removed from the early magnetite during the reactions (Hu et al. 2015).

Dissolution and precipitation reactions can be affected by fluid composition, solubility of mineral phases, temperature and pressure, Eh, and pH (Whitney et al. 1985; Hemley and Hunt 1992; Putnis 2002; Putnis and Putnis 2007). It is suggested that the higher contents of small ionic radius cations such as Si^{4+} in early magnetite make the magnetite more susceptible to fluid-assisted alteration because incorporation of these elements in magnetite would cause lattice defects or deformation (Huberty et al. 2012; Hu et al. 2014). The isomorphous replacement of Fe^{3+} by Si^{4+} in the tetrahedral sites of Si-rich magnetite in the Yamansu deposit has been demonstrated in recent studies (Li et al. 2017). Infiltration of mixed basinal brine and meteoric water that had dissolved evaporites can be an important process changing the physicochemical parameters of hydrothermal fluids, which led to the dissolution and precipitation of magnetite (Hu et al. 2014; Heidarian et al. 2016). These high-salinity, Cl^--rich ore-forming fluids enhance Fe solubility and disequilibrium between magnetite and evolving surficial fluids (Chou and Eugster 1977; Whitney et al. 1985; Hemley and Hunt 1992). However, pyrite associated with magnetite has $\delta^{34}S$ values ranging from − 2.2 to + 2.9‰, and H_2S in equilibrium with pyrite has $\delta^{34}S$ values of − 3.1 to + 2‰, precluding dissolved evaporite in the hydrothermal fluids. Alternatively, the variations in physicochemical conditions of fluids may be more important, which has been demonstrated by oscillatory zoning in magnetite (Fig. 9a, b). Carbon and oxygen isotope compositions of calcite suggest the involvement of meteoric water in the late mineralization process. Therefore, further dilution of magmatic-hydrothermal fluids by meteoric water in the late mineralization stage may induce the decline of temperature and pressure, which contributes to the dissolution of early magnetite and precipitation of late magnetite.

Origin and evolution of fluids

Sulfur isotope data of pyrite and the carbon and oxygen isotope data of calcite provide important constraints on the origin and evolution of the hydrothermal fluids. Sulfur in equilibrium with pyrite has $\delta^{34}S$ values of − 3.1 to + 2‰ with an average of − 0.8‰, suggesting magma-derived sulfur (Ohmoto 1972). Stage II calcite has C and O isotope composition similar to primary carbonate (Fig. 8a), whereas carbon has an isotope composition close to mantle CO_2 (Fig. 8b), indicating the derivation of C and O from magmatic-hydrothermal fluids. Fluids in equilibrium with stage II calcite have O isotope composition slightly higher than magmatic water, similar to those of formation and metamorphic water (Fig. 8c). Fluids in equilibrium with magnetite and calcite have $\delta^{18}O_{fluid}$ values of 12.2–12.5 and 8.3–12.2‰,

respectively (Zhang and Zhang 1996), also slightly higher than those of magmatic water (6–10‰; Taylor 1986) but similar to those of metamorphic water (5–25‰; Taylor 1974). Due to lack of regional metamorphism in the Aqishan-Yamansu belt, we infer that metamorphic water-like O isotope composition is more likely due to the fluid-rock interaction between magma-derived hydrothermal fluids with limestone because sedimentary materials are enriched in the heavy O isotope (Fig. 8a). Stage IV fluids have C isotope composition similar to average inorganic crustal CO_2 (Fig. 8c) but have O values similar to meteoric water (Fig. 8c), indicating that meteoric water was involved in the hydrothermal fluids during the later stage.

Pyrite samples have variable Re and common Os contents ranging from 105 to 426 ppb and from 26 to 776 ppt, respectively. Variable Re and Os contents of pyrite cannot be due to the derivation of Re and Os from different sources in view of the well-fitted isochron. This variability may reflect fluid evolution due to the change of redox conditions and ligand chemistry with time or in different portions of the deposit (e.g., Morelli et al. 2004), or it may be due to co-precipitated sulfides such as chalcopyrite. The initial Os isotope ratio is an important parameter to evaluate the relative contributions of crust and mantle in the formation of ore deposits. The elevated $^{187}Os/^{188}Os$ ratio of the crust (~ 1.0–1.3) (Walker et al. 1991), compared to the mantle (~ 0.11–0.15) (Meisel et al. 2001), can be used to discern between these two reservoirs. The initial $^{187}Os/^{188}Os$ ratio from the pyrite isochron is 0.22 ± 0.28 (Fig. 6a). The large uncertainty of the initial ratio makes it difficult to discuss the source of Os and, by inference, ore-forming fluids. But the highest initial Os ratio is lower than 0.5 if we consider the error, which is lower than values of the typical crust. Therefore, we can infer that Os of pyrite is mainly mantle-derived and minor crustal Os may have been involved. The trace crustal Os may have derived from magma rather than sedimentary rocks by hydrothermal replacement because the Re-Os isotope system of pyrite was closed after mineralization as indicated by the isochron. This is consistent with the dominant magmatic-hydrothermal origin of ore-forming fluids indicated by C, O, and S isotopes. Moreover, the mixing of magmatic-hydrothermal fluids with meteoric water in the late hydrothermal stage did not produce a mixing trend in the Re-Os data which has been documented at the Grasberg porphyry stockwork Cu-Au mineralization in Indonesia, for instance (Mathur et al. 2005). This indicates that the dilution of magmatic-hydrothermal fluids by meteoric water did not reset but only slightly disturbed the pyrite Re-Os isotope system in terms of the large uncertainty of the initial Os isotope ratio.

The trace element composition of magnetite also records the nature of the ore-forming fluids. EPMA results show that dark magnetite has Ca+Al+Mn and Ti+V contents similar to those of skarn deposits, indicating their hydrothermal origin (Fig. 11b). Light magnetite has lower Ca+Al+Mn contents than dark magnetite and plots in the BIF field, inconsistent with the skarn origin (Fig. 11b). This indicates that the trace element composition of light magnetite is different from that of dark magnetite and thus cannot be used to discriminate the origin of magnetite. In the plots of Ca+Al+Mn versus Ti+V and Ni/(Cr+Mn) versus Ti+V (Fig. 14), magnetite grains without zoned textures lie in the skarn field, indicating a skarn origin (Fig. 14).

Iron enrichment mechanism in the Yamansu deposit

Iron accumulation in volcanic-hosted Fe deposits commonly involves the model of magmatic versus hydrothermal, or the combination of both. For instance, Knipping et al. (2015a, 2015b) postulated that a separated high-salinity fluid scavenged Fe in the form of $FeCl_2$ complexes from intermediate melts to form the Kiruna-type deposit of Los Colorados (Chile). Günther et al. (2017) proposed different origins of two groups of magnetite from the Zhibo and Chagangnuoer Fe deposits in Western Tianshan. An ortho-magmatic fluid (~ 800 °C) separated from an intermediate melt accounted for the early magnetite mineralization, whereas partial remobilization of iron from the proximal, ortho-magmatic orebodies and a subsequent distal reprecipitation was responsible for the later magnetite formation. These processes were driven by late-stage hydrothermal fluids originating from deep-seated granitic/granodioritic intrusions in the immediate vicinity. Both examples show that ortho-magmatic melts and fluids are important for the Fe accumulation in a volcanic-hosted arc setting.

The Yamansu deposit shares many similarities with calcic skarn Fe deposits in tectonic setting, metals, host rocks, alteration, mineral assemblages, and origin of ore-forming fluids (Online Resource 4). Skarn is widely distributed in this deposit and has a thickness of up to 50 m. The skarn displays zones with garnet in the center and chlorite-epidote-sulfide facies at the margin (Lu et al. 1995), similar to typical skarn deposits (Meinert et al. 2005). The Yamansu deposit has an andradite-grossular assemblage and Si-rich magnetite (Li 2012), also typical of skarn deposits (Meinert et al. 2005). The ore-forming fluids are mainly magmatic water with minor meteoric water. The trace element composition of magnetite also indicates a skarn origin (Fig. 14). Because the majority of orebodies are hosted in skarn, iron enrichment in the Yamansu deposit is similar to that in skarn deposits elsewhere.

It is noteworthy that in addition to the skarn-related orebodies, there are also iron-rich fragments in the ignimbrite, volcanic breccia, and sedimentary volcanic breccia near the orebodies (Li et al. 2015). Iron-rich fragments are composed of mainly magnetite with various amounts of oligoclase, albite, and K-feldspar and have an average total Fe content of 26 wt%. These fragments were probably derived from iron-rich melts produced by the Fenner-type magma evolution that iron enrichment trends in residual basaltic liquids during magma differentiation (Fenner 1929; Li et al. 2015). Magnetite in these fragments is magmatic in origin as deduced from high Ti+V contents. Li et al. (2015) proposed that iron enrichment in Yamansu resulted from dissolution-precipitation of early magmatic magnetite by

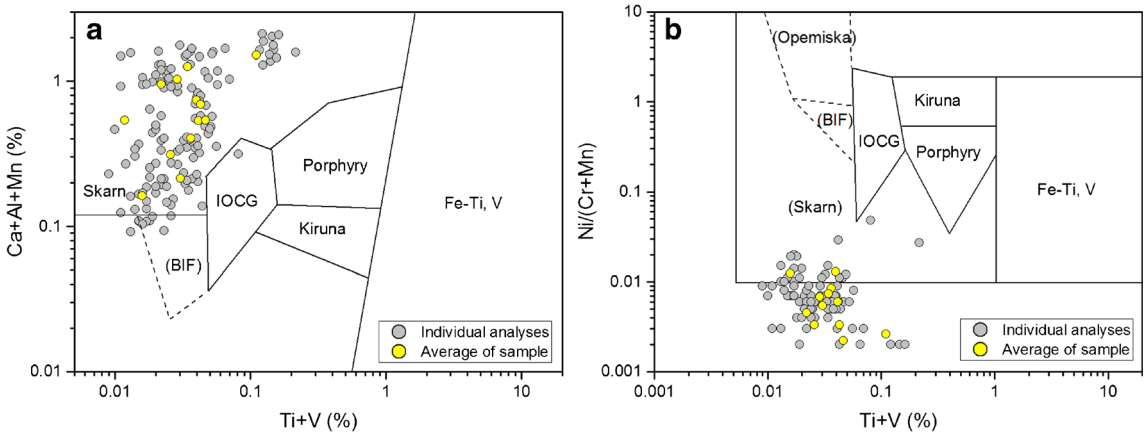

Fig. 14 Plots of Ca+Al+Mn versus Ti+V (**a**) and Ni/(Cr+Mn) versus Ti+V (**b**) for LA-ICP-MS data of magnetite without zoned textures. Both individual analyses and average of a single sample are shown for comparison. Reference fields are from Dupuis and Beaudoin (2011) and the abbreviations of deposit types are similar to those in Fig. 11b

late hydrothermal fluids. However, there is no evidence for the magmatic precursor in magnetite. Therefore, the iron enrichment model in the Zhibo and Chagangnuoer iron deposits cannot be used in Yamansu. By comparing the trace element composition of dark Si-rich magnetite and light Si-poor magnetite, we propose a possible model for the iron enrichment in the Yamansu deposit. Si-rich dark magnetite was possibly formed from Si ± Fe-rich magmatic-derived fluids due to large fluid-rock ratios at the temperature of skarn formation (~400 °C) (Meinert et al. 2005). Infiltration or dilution of magmatic-dominant fluids by meteoric water leads to variations in temperature and pressure of fluids, which induces the dissolution of early dark magnetite and precipitation of late magnetite. At the same time, fluctuating fluid composition and physicochemical conditions also resulted in the formation of zoned magnetite with oscillatory zoning. During this process, Si, Ca, Al, and Mn were removed from the dark magnetite, and thus, FeO contents were elevated (Fig. 11b, c). The iron enrichment mechanism by dissolution and precipitation processes was also proposed for the Chenchao skarn deposit in the middle-lower Yangtze River metallogenic belt (Hu et al. 2014). Therefore, we suggest that iron in the Yamansu deposit was mainly derived from magmatic-hydrothermal fluids similar to skarn deposits and further iron enrichment was due to dissolution and precipitation of early Si-rich skarn magnetite during the retrograde evolution of the skarn system.

Implication for regional mineralization

Previous studies concluded that hydrothermal iron mineralization in the ETOB mainly occurred in the late Carboniferous (~300 Ma) based on the ages of the Heifengshan, Shuangfengshan, and Shaquanzi Fe deposits (Huang et al. 2013a, 2014b). The ~300-Ma hydrothermal event is also indicated by other iron deposits such as the Bailingshan and Hongyuntan deposits. The Bailingshan deposit has a pyrite Rb-Sr age of 293 ± 10 Ma (Wang et al. 2015), whereas the Hongyuntan deposit has a mineralization age between ~324 and 300 Ma constrained by quartz keratophyre wall rock and granitic intrusions (Zheng 2015). Mao et al. (2005) suggested that the skarn Fe mineralization in the ETOB may have begun in the early Carboniferous (~350 Ma) and ended in the late Carboniferous (~290 Ma). Our Re-Os dating of pyrite from the Yamansu deposit indicates a ~320-Ma hydrothermal event for iron mineralization. Therefore, we suggest that hydrothermal iron mineralization in the ETOB occurred in multiple episodes peaking at ca. 320 Ma and ca. 300 Ma. Magmatic activities in the ETOB are characterized by minor Permian mafic and ultramafic intrusions in the Kanggurtag belt and numerous granitic intrusions in all belts of the ETOB. These granitoids have ages ranging from ~230 to ~386 Ma (Tong et al. 2010; Zhou et al. 2010) and two peak ages of 340–310 and 300–270 Ma (Online Resource 6). The two ages of iron mineralization (~320 and ~300 Ma) overlap with the two ages of granitic magmatism, indicating that iron mineralization in ETOB is the product of intense granitic magmatic activity although skarn Fe deposits are commonly associated with gabbroic to syenitic intrusions (Online Resource 4).

Calcic Fe skarns are associated with Fe-rich plutons intruded into limestone and volcanic wall rocks (Meinert et al. 2005). Skarns are commonly developed in the carbonated layers of the country rock and about 85% of skarns occur within 800 m of an intrusive contact. However, skarns can spread quite far from the intrusion (up to several kilometers) if there is fluid flow (Meinert 1992). As discussed above, magnetite formation in the Yamansu deposit involves fluid infiltration processes. Skarns in Yamansu, thus, are possibly disconnected distal skarns in the pluton-related skarn system. A subsequent distal reprecipitation of hydrothermal Fe orebodies and related skarn possibly explains volcanic-hosted skarn deposits lacking proximal intrusions. This metallogenetic model is very useful for the understanding of similar deposits. For example, the Cihai and Cinan Fe deposits in the Beishan area adjacent to the ETOB are considered to be

magmatic (Wang et al. 2008; Tang et al. 2017) or hydrothermal (skarn) in origin (Huang et al. 2013c; Zheng et al. 2017). These deposits may have involved both magmatic and hydrothermal processes, in which hydrothermal magnetite may represent a distal Fe component.

Conclusions

The Yamansu deposit has mineral associations, related alteration, and styles of mineralization similar to Fe skarn deposits elsewhere. The deposit was formed at ~ 320 Ma and derived from dominantly magmatic-hydrothermal fluids with minor meteoric water. Some magnetite grains are composed of dark and light domains in BSE images. Light magnetite may have formed via a process of replacement of dark magnetite due to a dissolution-reprecipitation process. Dilution of magmatic-hydrothermal fluids by meteoric water could be responsible for this process. Trace element compositions of magnetite imply a skarn origin. We suggest that iron in the Yamansu deposit was mainly derived from magmatic-hydrothermal fluids similar to skarn deposits and further iron enrichment was due to dissolution and precipitation of early skarn magnetite by external fluids. The Yamansu deposit may represent a distal skarn deposit, in which skarn and related Fe orebodies possibly represent the distal expression of a pluton-related skarn system.

Acknowledgments Field work was helped by staff of the Yamansu deposit. Zengsheng Li and Zhihui Dai are thanked for EPMA and LA-ICP-MS analyses, respectively. Ning An and Jing Gu are thanked for stable isotope analyses. We also thank the two editors (Bernd Lehmann and Ruizhong Hu), Ryan Mathur, and an anonymous reviewer who significantly improved the manuscript.

Funding information This work was jointly supported by grants from the National Natural Science Foundation of China (41503039 and 41673050), the Chinese 973 project (2012CB416804), and the "CAS Hundred Talents" Project to J.F. Gao (Y5CJ038000).

References

Barra F, Reich M, Selby D, Rojas P, Simon A, Salazar E, Palma G (2017) Unraveling the origin of the Andean IOCG clan: a Re-Os isotope approach. Ore Geol Rev 81:62–78

Brenan JM, Cherniak DJ, Rose LA (2000) Diffusion of osmium in pyrrhotite and pyrite: implications for closure of the Re-Os isotopic system. Earth Planet Sci Lett 180(3–4):399–413. https://doi.org/10.1016/S0012-821X(00)00165-5

Che ZC, Liu HF, Liu L (1994) The formation of evolution of central Tianshan Orogenic Belt. Geological Publishing House, Beijing (in Chinese)

Chou I-M, Eugster HP (1977) Solubility of magnetite in supercritical chloride solutions. Am J Sci 277(10):1296–1314. https://doi.org/10.2475/ajs.277.10.1296

Ciobanu CL, Cook NJ (2004) Skarn textures and a case study: the Ocna de Fier-Dognecea orefield, Banat, Romania. Ore Geol Rev 24(3–4):315–370. https://doi.org/10.1016/j.oregeorev.2003.04.002

Clark I, Fritz P (1997) Environmental isotopes in hydrogeology. Lewis, New York

Dare SAS, Barnes S-J, Beaudoin G, Méric J, Boutroy E, Potvin-Doucet C (2014) Trace elements in magnetite as petrogenetic indicators. Mineral Deposita 49(7):785–796. https://doi.org/10.1007/s00126-014-0529-0

Dare SA, Barnes S-J, Beaudoin G (2015) Did the massive magnetite "lava flows" of El Laco (Chile) form by magmatic or hydrothermal processes? New constraints from magnetite composition by LA-ICP-MS. Mineral Deposita 50(5):607–617. https://doi.org/10.1007/s00126-014-0560-1

Davies J (2010) Re-Os geochronology of oxide minerals. Master thesis, University of Alberta, Edmonton

Ding TP, Vaikiers S, Wan DF, Bai RM, Zou XQ, Li YH, Zhang QL, Bievre PD (2001) The $\delta^{33}S$ and $\delta^{34}S$ values and absolute $^{32}S/^{33}S$ and $^{32}S/^{34}S$ ratios of IAEA and Chinese sulfur isotope reference materials. Bull China Soc Miner Petrol Geochem 20:425–427 (in Chinese with English abstract)

Dupuis C, Beaudoin G (2011) Discriminant diagrams for iron oxide trace element fingerprinting of mineral deposit types. Mineral Deposita 46(4):319–335

Einaudi MT, Meinert LD, Newberry RJ (1981) Skarn deposits. Econ Geol 75:317–391

Fenner CN (1929) The crystallization of basalts. Am J Sci 18:225–253

Gao ZJ, Chen JX, Lu SN (1993) Precambrian geology of northern Xinjiang. Geological Publishing House, Beijing (in Chinese)

Gao J, Li MS, Xiao XC, Tang YQ, He GQ (1998) Paleozoic tectonic evolution of the Tianshan Orogen, northwestern China. Tectonophysics 287(1–4):213–231. https://doi.org/10.1016/S0040-1951(97)00211-4

Gao J-F, Zhou M-F, Light Foot PC, Wang CY, Qi L, Sun M (2013) Sulfide saturation and magma emplacement in the formation of the Permian Huangshandong Ni-Cu sulfide deposit, Xinjiang, northwestern China. Econ Geol 108(8):1833–1848. https://doi.org/10.2113/econgeo.108.8.1833

Günther T, Klemd R, Zhang X, Horn I, Weyer S (2017) In-situ trace element and Fe-isotope studies on magnetite of the volcanic-hosted Zhibo and Chagangnuoer iron ore deposits in the Western Tianshan, NW China. Chem Geol 453:111–127

Han BF, Ji JQ, Song B, Chen LH, Li ZH (2004) SHRIMP zircon U-Pb ages of Kalatongke No. 1 and Huangshandong Cu-Ni-bearing mafic-ultramafic complexes, North Xinjiang, and geological implications. Chin Sci Bull 49:2424–2429

He GQ, Li MS, Liu DQ (1994) Paleozoic crustal evolution and mineralization in Xinjiang of China. Xinjiang People's Publishing House, Urimqi (in Chinese)

Heidarian H, Lentz D, Alirezaei S, Peighambari S, Hall D (2016) Using the chemical analysis of magnetite to constrain various stages in the formation and genesis of the Kiruna-type chadormalu magnetite-apatite deposit, Bafq district, Central Iran. Mineral Petrol 110(6):927–942

Hemley JJ, Hunt JP (1992) Hydrothermal ore-forming processes in the light of studies in rock-buffered systems; II, some general geologic applications. Econ Geol 87(1):23–43. https://doi.org/10.2113/gsecongeo.87.1.23

Henriquez F, Martin RF (1978) Crystal-growth textures in magnetite flows and feeder dykes, El Laco, Chile. Can Mineral 16:581–589

Hoefs J (1997) Stable isotope geochemistry. Springer, Heidelberg. https://doi.org/10.1007/978-3-662-03377-7

Hou T, Zhang Z, Pirajno F, Santosh M, Encarnacion J, Liu J, Zhao Z, Zhang L (2014a) Geology, tectonic settings and iron ore metallogenesis associated with submarine volcanism in China: an overview. Ore Geol Rev 57:498–517. https://doi.org/10.1016/j.oregeorev.2013.08.007

Hou T, Zhang Z, Santosh M, Encarnacion J, Zhu J, Luo W (2014b) Geochronology and geochemistry of submarine volcanic rocks in the Yamansu iron deposit, Eastern Tianshan Mountains, NW China: constraints on the metallogenesis. Ore Geol Rev 56:487–502. https://doi.org/10.1016/j.oregeorev.2013.03.008

Hu H, Li J-W, Lentz D, Ren Z, Zhao X-F, Deng X-D, Hall D (2014) Dissolution–reprecipitation process of magnetite from the Chengchao iron deposit: insights into ore genesis and implication for *in-situ* chemical analysis of magnetite. Ore Geol Rev 57:393–405. https://doi.org/10.1016/j.oregeorev.2013.07.008

Hu H, Lentz D, Li J-W, McCarron T, Zhao X-F, Hall D (2015) Reequilibration processes in magnetite from iron skarn deposits. Econ Geol 110(1):1–8. https://doi.org/10.2113/econgeo.110.1.1

Huang X-W, Qi L, Gao J-F, Zhou M-F (2013a) First reliable Re-Os ages of pyrite and stable isotope compositions of Fe(-Cu) deposits in the Hami region, Eastern Tianshan Orogenic Belt, NW China. Resour Geol 63(2):166–187. https://doi.org/10.1111/rge.12003

Huang X-W, Zhao X-F, Qi L, Zhou M-F (2013b) Re-Os and S isotopic constraints on the origins of two mineralization events at the Tangdan sedimentary rock-hosted stratiform Cu deposit, SW China. Chem Geol 347:9–19. https://doi.org/10.1016/j.chemgeo.2013.03.020

Huang X-W, Zhou M-F, Qi L, Gao J-F, Wang Y-W (2013c) Re-Os isotopic ages of pyrite and chemical composition of magnetite from the Cihai magmatic-hydrothermal Fe deposit, NW China. Mineral Deposita 48(8):925–946. https://doi.org/10.1007/s00126-013-0467-2

Huang X, Qi L, Meng Y (2014a) Trace element geochemistry of magnetite from the Fe(-Cu) deposits in the Hami region, Eastern Tianshan Orogenic Belt, NW China. Acta Geol Sin 88:176–195

Huang XW, Qi L, Wang YC, Liu YY (2014b) Re-Os dating of magnetite from the Shaquanzi Fe-Cu deposit, eastern Tianshan, NW China. Sci China Earth Sci 57(2):267–277. https://doi.org/10.1007/s11430-013-4660-z

Huang X-W, Gao J-F, Qi L, Zhou M-F (2015) In-situ LA-ICP-MS trace elemental analyses of magnetite and Re–Os dating of pyrite: the Tianhu hydrothermally remobilized sedimentary Fe deposit, NW China. Ore Geol Rev 65:900–916. https://doi.org/10.1016/j.oregeorev.2014.07.020

Huberty JM, Konishi H, Heck PR, Fournelle JH, Valley JW, Xu H (2012) Silician magnetite from the Dales Gorge Member of the Brockman Iron Formation, Hamersley Group, Western Australia. Am Mineral 97(1):26–37. https://doi.org/10.2138/am.2012.3864

Jahn B, Wu F, Chen B (2000) Granitoids of the central Asian Orogenic Belt and continental growth in the Phanerozoic. Trans R Soc Edinb Earth Sci 91(1–2):181–194. https://doi.org/10.1017/S0263593300007367

Ji JS, Tao HX, Zeng ZR, Yang XK, Zhang LC (1994) Geology and mineralization of the Kangurtag gold belt in Eastern Tianshan. Geological Publishing House, Beijing (in Chinese)

Jiang FZ (1983) A discussion on genetic types and metallogenic characteristics of the marine volcanic iron and/or copper deposits in China. Mineral Deps 2(4):11–18 (in Chinese with English abstract)

Jiang FZ, Wang YW (2005) Marine volcanic rocks and related metallic ore deposits. Metallurgical Industry Press, Beijing (in Chinese)

Kajiwara Y (1971) Sulfur isotope study of the Kuroko-ores of the Shakanai No. l deposits, Akita Prefecture, Japan. Geochem J 4(4):157–181. https://doi.org/10.2343/geochemj.4.157

Knipping JL, Bilenker LD, Simon AC, Reich M, Barra F, Deditius AP, Lundstrom C, Bindeman I, Munizaga R (2015a) Giant Kiruna-type deposits form by efficient flotation of magmatic magnetite suspensions. Geology 43(7):591–594. https://doi.org/10.1130/G36650.1

Knipping JL, Bilenker LD, Simon AC, Reich M, Barra F, Deditius AP, W lle M, Heinrich CA, Holtz F, Munizaga R (2015b) Trace elements in magnetite from massive iron oxide-apatite deposits indicate a combined formation by igneous and magmatic-hydrothermal processes. Geochim Cosmochim Acta 171:15–38. https://doi.org/10.1016/j.gca.2015.08.010

Li G (2012) Iron ore deposits in the eastern Tianshan Orogenic Belt (China): the magnetite-skarn-magmatism association. PhD thesis, University of Orleans

Li HQ, Chen FW (2003) Isotopic geochronology of regional mineralization in Xinjiang, NW China. Geological Publishing House, Beijing (in Chinese)

Li W, Chen G, Sun S (1986) A study of the mineral paragensis of Yamansu iron deposit. Explor Nat 5:119–125 (in Chinese with English abstract)

Li Y, Yang JS, Zhang J, Li TF, Chen SY, Ren YF, Xu XZ (2011) Tectonical significance of Carboniferous volcanics in eastern Tianshan. Acta Petrol Sin 27:193–209 (in Chinese with English abstract)

Li HM, Ding JH, Li LX, Yao T (2014) The genesis of the skarn and the genetic type of the Yamansu iron deposit, eastern Tianshan, Xinjiang. Acta Geol Sin 88:2477–2489 (in Chinese with English abstract)

Li H-M, Ding J-H, Zhang Z-C, Li L-X, Chen J, Yao T (2015) Iron-rich fragments in the Yamansu iron deposit, Xinjiang, NW China: constraints on metallogenesis. J Asian Earth Sci 113:1068–1081. https://doi.org/10.1016/j.jseaes.2015.06.026

Li G, Gou F, Wu C, Dong B (2017) Status of silicon in magnetite. Acta Geol Sin 91(2):731–732. https://doi.org/10.1111/1755-6724.13130

Liu Y, Hu Z, Gao S, Günther D, Xu J, Gao C, Chen H (2008) *In situ* analysis of major and trace elements of anhydrous minerals by LA-ICP-MS without applying an internal standard. Chem Geol 257(1–2):34–43. https://doi.org/10.1016/j.chemgeo.2008.08.004

Lu DR, Ji JS, Lv RS, Tao HX (1995) Geochemical characteristics and ore genesis of the Yamansu deposit in Xinjiang. Northwest Geol 16:15–19 (in Chinese)

Ludwig KR (1980) Calculation of uncertainties of U-Pb isotope data. Earth Planet Sci Lett 46(2):212–220. https://doi.org/10.1016/0012-821X(80)90007-2

Ludwig KR (2003) Isoplot/Ex version 3.23. A geochronological toolkit for Microsoft Excel. Berkeley Geochronology Center Special Publication

Luo T, Liao Q-A, Chen J-P, Zhang X-H, Guo D-B, Hu Z-C (2012) LA-ICP-MS zircon U-Pb dating of the volcanic rocks from Yamansu Formation in the eastern Tianshan, and its geological significance. Earth Sci J Chin Univ Geosci 37:1338–1352 (in Chinese with English abstract)

Ma RS, Shu LS, Sun JQ (1997) Tectonic evolution and mineralization of eastern Tianshan. Geological Publishing House, Beijing (in Chinese)

Makvandi S, Beaudoin G, McClenaghan BM, Layton-Matthews D (2015) The surface texture and morphology of magnetite from the Izok Lake volcanogenic massive sulfide deposit and local glacial sediments, Nunavut, Canada: application to mineral exploration. J Geochem Explor 150:84–103. https://doi.org/10.1016/j.gexplo.2014.12.013

Makvandi S, Ghasemzadeh-Barvarz M, Beaudoin G, Grunsky EC, McClenaghan MB, Duchesne C, Boutroy E (2016) Partial least squares-discriminant analysis of trace element compositions of magnetite from various VMS deposit subtypes: application to mineral exploration. Ore Geol Rev 78:388–408. https://doi.org/10.1016/j.oregeorev.2016.04.014

Mao JW, Goldfarb RJ, Wang YT, Hart CJ, Wang ZL, Yang JM (2005) Late Paleozoic base and precious metal deposits, east Tianshan, Xinjiang, China: characteristics and geodynamic setting. Episodes 28:23–30

Mathur R, Marschik R, Ruiz J, Munizaga F, Leveille RA, Martin W (2002) Age of mineralization of the Candelaria Fe oxide Cu-Au deposit and the origin of the Chilean iron belt, based on Re-Os isotopes. Econ Geol 97(1):59–71. https://doi.org/10.2113/gsecongeo.97.1.59

Mathur R, Titley S, Ruiz J, Gibbins S, Friehauf K (2005) A Re-Os isotope study of sedimentary rocks and copper-gold ores from the Ertsberg District, West Papua, Indonesia. Ore Geol Rev 26:207–226

Meinert LD (1992) Skarns and skarn deposits. Geosci Can 19:145–162

Meinert LD, Dipple GM, Nicolescu S (2005) World skarn deposits. In: Hedenquist JW, Thompson JFH, Goldfarb RJ, Richards JP (eds)

Economic Geology 100th Anniversary Volume. Society of Economic Geologists, Littleton, pp 299–336

Meisel T, Walker RJ, Irving AJ, Lorand J-P (2001) Osmium isotopic compositions of mantle xenoliths: a global perspective. Geochim Cosmochim Acta 65(8):1311–1323. https://doi.org/10.1016/S0016-7037(00)00566-4

Morelli RM, Creaser RA, Selby D, Kelley KD, Leach DL, King AR (2004) Re-Os sulfide geochronology of the Red Dog sediment-hosted Zn-Pb-Ag deposit, Brooks Range, Alaska. Econ Geol 99(7):1569–1576. https://doi.org/10.2113/gsecongeo.99.7.1569

Nadoll P, Mauk JL, Hayes TS, Koenig AE, Box SE (2012) Geochemistry of magnetite from hydrothermal ore deposits and host rocks of the Mesoproterozoic Belt Supergroup, United States. Econ Geol 107(6):1275–1292. https://doi.org/10.2113/econgeo.107.6.1275

Nadoll P, Angerer T, Mauk JL, French D, Walshe J (2014) The chemistry of hydrothermal magnetite: a review. Ore Geol Rev 61:1–32

Nelson DR, Chivas AR, Chappell BW, McCulloch MT (1988) Geochemical and isotopic systematics in carbonatites and implications for the evolution of ocean-island sources. Geochim Cosmochim Acta 52(1):1–17. https://doi.org/10.1016/0016-7037(88)90051-8

Nold JL, Dudley MA, Davidson P (2014) The Southeast Missouri (USA) Proterozoic iron metallogenic province—types of deposits and genetic relationships to magnetite–apatite and iron oxide–copper–gold deposits. Ore Geol Rev 57:154–171. https://doi.org/10.1016/j.oregeorev.2013.10.002

Nyström JO, Henríquez F (1994) Magmatic features of iron ores of the Kiruna type in Chile and Sweden; ore textures and magnetite geochemistry. Econ Geol 89(4):820–839. https://doi.org/10.2113/gsecongeo.89.4.820

Nyström JO, Billström K, Henríquez F, Fallick AE, Naslund HR (2008) Oxygen isotope composition of magnetite in iron ores of the Kiruna type in Chile and Sweden. GFF 130(4):177–188. https://doi.org/10.1080/11035890809452771

Ohmoto H (1972) Systematics of sulfur and carbon isotopes in hydrothermal ore deposits. Econ Geol 67(5):551–578. https://doi.org/10.2113/gsecongeo.67.5.551

Ohmoto H (1986) Stable isotope geochemistry of ore deposits. In: Valley JW, Taylor HPJ, O'Neil JR (eds) Reviews in mineralogy, vol 16. Stable isotopes on high temperature geological process. Mine Soc Am, pp 491–559

Ohmoto H, Rye RO (1979) Isotopes of sulfur and carbon. Geochemistry of hydrothermal ore deposits. Wiley, New York

Pirajno F (2010) Intracontinental strike-slip faults, associated magmatism, mineral systems and mantle dynamics: examples from NW China and Altay-Sayan (Siberia). J Geodyn 50(3–4):325–346. https://doi.org/10.1016/j.jog.2010.01.018

Putnis A (2002) Mineral replacement reactions: from macroscopic observations to microscopic mechanisms. Mineral Mag 66(5):689–708. https://doi.org/10.1180/0026461026650056

Putnis A (2009) Mineral replacement reactions. Rev Mineral Geochem 70(1):87–124. https://doi.org/10.2138/rmg.2009.70.3

Putnis A, John T (2010) Replacement processes in the Earth's crust. Elements 6(3):159–164. https://doi.org/10.2113/gselements.6.3.159

Putnis A, Putnis CV (2007) The mechanism of reequilibration of solids in the presence of a fluid phase. J Solid State Chem 180(5):1783–1786. https://doi.org/10.1016/j.jssc.2007.03.023

Qi L, Zhou M-F, Wang CY, Sun M (2007) Evaluation of a technique for determining Re and PGEs in geological samples by ICP-MS coupled with a modified Carius tube digestion. Geochem J 41(6):407–414. https://doi.org/10.2343/geochemj.41.407

Qi L, Zhou M-F, Gao J, Zhao Z (2010) An improved Carius tube technique for determination of low concentrations of Re and Os in pyrites. J Anal At Spectrom 25(4):585–589. https://doi.org/10.1039/b919016c

Qi L, Gao J-F, Zhou M-F, Hu J (2013) The design of re-usable Carius tubes for the determination of rhenium, osmium and platinum-group elements in geological samples. Geostand Geoanal Res 37(3):345–351. https://doi.org/10.1111/j.1751-908x.2012.00211.x

Qin KZ, Fang TH, Wang SL, Zhu BQ, Feng YM, Yu HF, Xiu QY (2002) Plate tectonics division, evolution and metallogenic settings in eastern Tianshan Mountains, NW China. Xinjiang Geol 20:302–308 (in Chinese with English abstract)

Qin KZ, Zhang LC, Xiao WJ, Xu XW, Yan Z, Mao JW (2003) Overview of major Au, Cu, Ni and Fe deposits and metallogenic evolution of the eastern Tianshan Mountains, northwestern China. In: Mao JW, Goldfarb RJ, Seltmann R, Wang DH, Xiao WJ, Hart CJ (eds) Tectonic evolution and metallogeny of the Chinese Altay and Tianshan. IAGOD guidebook series 10. CERCAMS/NHM, London, pp 227–248

Rangarajan R, Ghosh P (2011) Role of water contamination within the GC column of a GasBench II peripheral on the reproducibility of $^{18}O/^{16}O$ ratios in water samples. Isot Environ Health Stud 47(4):498–511. https://doi.org/10.1080/10256016.2011.631007

Ray JS, Ramesh R, Pande K (1999) Carbon isotopes in Kerguelen plume-derived carbonatites: evidence for recycled inorganic carbon. Earth Planet Sci Lett 170:205–214

Rhodes AL, Oreskes N, Sheets S (1999) Geology and rare earth element geochemistry of magnetite deposits at El Laco, Chile. In: Skinner BJ (ed) Geology and ore deposits of the Central Andes. Special Publication 7, Soc Econ Geol, pp 299–332

Schoenberg R, Nägler TF, Kramers JD (2000) Precise Os isotope ratio and Re-Os isotope dilution measurements down to the picogram level using multicollector inductively coupled plasma mass spectrometry. Int J Mass Spectrom 197(1–3):85–94. https://doi.org/10.1016/S1387-3806(99)00215-8

Selby D, Kelley KD, Hitzman MW, Zieg J (2009) Re-Os sulfide (bornite, chalcopyrite, and pyrite) systematics of the carbonate-hosted copper deposits at Ruby Creek, southern Brooks range, Alaska. Econ Geol 104(3):437–444. https://doi.org/10.2113/gsecongeo.104.3.437

Sengör AMC, Burtman VS (1993) Evolution of the Altaid tectonic collage and Palaeozoic crustal growth in Eurasia. Nature 364(6435):299–307. https://doi.org/10.1038/364299a0

Shimazaki H (1998) On the occurrence of Silician magnetites. Resour Geol 48(1):23–29. https://doi.org/10.1111/j.1751-3928.1998.tb00004.x

Shu LS, Charvet J, Lu HF, Laurent-Charvet S (2002) Paleozoic accretion-collision events and kinematics of deformation in the eastern part of the southern-central Tianshan belt, China. Acta Geol Sin 76:308–323

Sillitoe RH, Burrows DR (2002) New field evidence bearing on the origin of the El Laco magnetite deposit, northern Chile. Econ Geol 97:1101–1109

Stein HJ, Morgan JW, Scherstén A (2000) Re-Os dating of low-level highly radiogenic (LLHR) sulfides: the Harnäs gold deposit, southwest Sweden, records continental-scale tectonic events. Econ Geol 95:1657–1671

Tang D, Qin K, Chen B, Mao Y, Guo H, Evans NJ (2017) Mineral chemistry and genesis of the Permian Cihai and Cinan magnetite deposits, Beishan, NW China. Ore Geol Rev 86:79–99. https://doi.org/10.1016/j.oregeorev.2017.01.019

Taylor HP (1974) The application of oxygen and hydrogen isotope studies to problems of hydrothermal alteration and ore deposition. Econ Geol 69(6):843–883. https://doi.org/10.2113/gsecongeo.69.6.843

Taylor BE (1986) Magmatic volatiles: isotope variation of C, H and S. In: Reviews in mineralogy, vol 16. Stable isotopes on high temperature geological process. Miner Soc Am, pp 185–226

Tong Y, Wang T, Hong DW, Han BF, Zhang JJ, Shi XJ, Wang C (2010) Spatial and temporal distribution of the Carboniferous-Permian granitoids in northern Xinjiang and its adjacent areas, and its tectonic significance. Acta Petrol Miner 29:619–641 (in Chinese with English abstract)

Tornos F, Velasco F, Hanchar JM (2016) Iron-rich melts, magmatic magnetite, and superheated hydrothermal systems: the El Laco deposit, Chile. Geology 44:427–430

Valley JW (1986) Stable isotope geochemistry of metamorphic rocks. In: Valley JW, Taylor HPJ, O'Neil JR (eds) Reviews in mineralogy and geochemistry, vol 16. Stable isotopes on high temperature geological process. Miner Soc Am, pp 445–489

Walker RJ, Morgan JW, Naldrett AJ, Li C, Fassett JD (1991) Re-Os isotope systematics of Ni-Cu sulfide ores, Sudbury Igneous Complex, Ontario: evidence for a major crustal component. Earth Planet Sci Lett 105(4):416–429. https://doi.org/10.1016/0012-821X(91)90182-H

Wang YW, Wang JB, Wang LJ, Qin QX, Peng XM, Hui WD (2005) Weiya vanadium-bearing titanomagnetite deposit in Xinjiang: a polygenetic magmatic differentiation-magmatic injection-magmatic hydrothermal deposit. Mineral Deps 24:349–360 (in Chinese with English abstract)

Wang DH, Li CJ, Chen ZH, Chen SP, Xiao KY, Li HQ, Liang T (2006a) Metallogenic characteristics and direction in mineral research in east Tianshan, Xinjiang, China. Geol Bull Chin 25:910–915 (in Chinese with English abstract)

Wang JB, Wang YW, He ZJ (2006b) Ore deposits as a guide to the tectonic evolution in the East Tianshan Mountains, NW China. Geol China 33:461–469 (in Chinese with English abstract)

Wang YW, Wang JB, Wang LJ, Long LL (2008) Metallogenic series related to Permian mafic complex in North Xinjiang: post-collisional stage or mantle plume result? Acta Geol Sin 82:788–795

Wang LS, Li HQ, Chen YC, Liu DQ (2015) Geological feature and mineralization epoch of Bailingshan iron deposit, Hami, Xinjiang, China. Mineral Deps 24:264–269 (in Chinese with English abstract)

Westendorp RW, Watkinson DH, Jonasson IR (1991) Silicon-bearing zoned magnetite crystals and the evolution of hydrothermal fluids at the Ansil Cu-Zn mine, Rouyn-Noranda, Quebec. Econ Geol 86(5):1110–1114. https://doi.org/10.2113/gsecongeo.86.5.1110

Whitney JA, Hemley JJ, Simon FO (1985) The concentration of iron in chloride solutions equilibrated with synthetic granitic compositions; the sulfur-free system. Econ Geol 80(2):444–460. https://doi.org/10.2113/gsecongeo.80.2.444

Windley BF, Alexeiev D, Xiao W, Kröner A, Badarch G (2007) Tectonic models for accretion of the central Asian Orogenic Belt. J Geol Soc 164:31–47

Wu C-Z, Lei R-X, Santosh M, Chi G-X, Gu L-X, Xie S-W (2016) Ordovician volcano–sedimentary iron deposits of the Eastern Tianshan area, Northwest China: the Tianhu example. Int Geol Rev 58(11):1398–1416. https://doi.org/10.1080/00206814.2016.1163516

Xia LQ, Xu XY, Xia ZC, Li XM, Ma ZP, Wang LS (2003) Carboniferous post-collisional rift volcanism of the Tianshan Mountains, northwestern China. Acta Geol Sin 77:338–360 (in Chinese with English abstract)

Xiao XC, Tang YQ, Feng YM, Zhu BQ, Li JY, Zhao M (1992) Tectonic evolution of the northern Xinjiang and its adjacent regions. Geological Publishing House, Beijing (in Chinese)

Xiao WJ, Zhang LC, Qin KZ, Sun S, Li JL (2004) Paleozoic accretionary and collisional tectonics of the Eastern Tianshan (China): implications for the continental growth of central Asia. Am J Sci 304(4):370–395. https://doi.org/10.2475/ajs.304.4.370

Xiao W, Han C, Yuan C, Sun M, Lin S, Chen H, Li Z, Li J, Sun S (2008) Middle Cambrian to Permian subduction-related accretionary orogenesis of northern Xinjiang, NW China: implications for the tectonic evolution of central Asia. J Asian Earth Sci 32:102–117

Xie W, Song XY, Deng YF, Wang YS, Ba DH, Zheng WQ, Li XB (2012) Geochemistry and petrogenetic implications of a Late Devonian mafic-ultramafic intrusion at the southern margin of the central Asian Orogenic Belt. Lithos 144–145:209–230. https://doi.org/10.1016/j.lithos.2012.03.010

Xu XW, Ma TL, Sun LQ, Cai XP (2003) Characteristics and dynamic origin of the large-scale Jiaoluotage ductile compressional zone in the eastern Tianshan Mountains, China. J Struct Geol 25(11):1901–1915. https://doi.org/10.1016/S0191-8141(03)00017-8

Yan WY (1985) The characteristics of early Carboniferous volcanic island arc and mineralization in the east section of Tianshan. Xinjiang Geol 3:49–51 (in Chinese with English abstract)

Yang XK, Tao HX, Luo GC, Ji JS (1996) Basic features of plate tectonics in east Tianshan of China. Xinjiang Geol 14:221–227 (in Chinese with English abstract)

Yang XK, Cheng HB, Ji JS, Cheng Q, Luo GC (1999) Analysis on gold and copper ore-forming system with collision orogeny of eastern Tianshan. Geotecton Metallog 23:315–332 (in Chinese with English abstract)

Yao PH, Wang KN, Dun CL, Lin ZT, Song X (1993) Records of China's iron ore deposits. Metallurgical Industry Press, Beijing (in Chinese with English abstract)

Zhang J, Zhang X (1996) Geological-geochemical features of Yamansu iron deposit in Hami. Xinjiang Geol 14:170–180 (in Chinese with English abstract)

Zhang Z, Gu L, Wu C, Li W, Xi A, Wang S (2005) Zircon SHRIMP dating for the Weiya pluton, eastern Tianshan: its geological implications. Acta Geol Sin 79:481–490

Zhang Z, Zhou G, Kusky TM, Yan S, Chen B, Zhao L (2009) Late Paleozoic volcanic record of the eastern Junggar terrane, Xinjiang, northwestern China: major and trace element characteristics, Sr-Nd isotopic systematics and implications for tectonic evolution. Gondwana Res 16(2):201–215. https://doi.org/10.1016/j.gr.2009.03.004

Zhang Z, Hou T, Santosh M, Li H, Li J, Zhang Z, Song X, Wang M (2014) Spatio-temporal distribution and tectonic settings of the major iron deposits in China: an overview. Ore Geol Rev 57:247–263. https://doi.org/10.1016/j.oregeorev.2013.08.021

Zhang X, Klemd R, Gao J, Dong L-H, Wang X-S, Haase K, Jiang T, Qian Q (2015) Metallogenesis of the Zhibo and Chagangnuoer volcanic iron oxide deposits in the Awulale Iron Metallogenic Belt, Western Tianshan orogen, China. J Asian Earth Sci 113(Part 1):151–172

Zheng RQ (2015) Geological feature and ore genesis of the Hongyuntan iron deposit in eastern Tianshan. China University of Geosciences (Beijing), Beijing, Xinjiang (in Chinese with English abstract)

Zheng J, Mao J, Yang F, Chai F, Zhu Y (2017) Mineralogy, fluid inclusions, and isotopes of the Cihai iron deposit, eastern Tianshan, NW China: implication for hydrothermal evolution and genesis of subvolcanic rocks-hosted skarn-type deposits. Ore Geol Rev 86:404–425

Zhou JY, Cui BF, Xiao HL, Chen SZ, Zhu DM (2001) Kangguertag-Huangshan collision zone of bilateral subduction and its metallogenic model and prognosis in Xinjiang, China. Volcanol Mineral Resour 22:252–263 (in Chinese with English Abstract)

Zhou MF, Michael Lesher C, Yang Z, Li J, Sun M (2004) Geochemistry and petrogenesis of 270 Ma Ni-Cu-(PGE) sulfide-bearing mafic intrusions in the Huangshan district, eastern Xinjiang, Northwest China: implications for the tectonic evolution of the central Asian orogenic belt. Chem Geol 209:233–257

Zhou TF, Yuan F, Zhang DY, Fan Y, Liu S, Peng MX, Zhang JD (2010) Geochronology, tectonic settings and mineraltion of granitoids in Jueluotage area, eastern Tianshan, Xinjiang. Acta Petrol Sin 26:478–502 (in Chinese with English abstract)